



**HAL**  
open science

## Incipient wolframite deposition at Panasqueira (Portugal): W-rutile and tourmaline compositions as proxies for early fluid composition

Eleonora Carocci, Christian Marignac, Michel Cathelineau, Laurent Truche,  
Marc Poujol, Marie-Christine Boiron, Filipe Pinto

### ► To cite this version:

Eleonora Carocci, Christian Marignac, Michel Cathelineau, Laurent Truche, Marc Poujol, et al.. Incipient wolframite deposition at Panasqueira (Portugal): W-rutile and tourmaline compositions as proxies for early fluid composition. *Economic Geology*, 2021, 16 (1), pp.123-146. 10.5382/econ-geo.4783 . insu-02965235

**HAL Id: insu-02965235**

**<https://insu.hal.science/insu-02965235>**

Submitted on 14 Oct 2020

**HAL** is a multi-disciplinary open access archive for the deposit and dissemination of scientific research documents, whether they are published or not. The documents may come from teaching and research institutions in France or abroad, or from public or private research centers.

L'archive ouverte pluridisciplinaire **HAL**, est destinée au dépôt et à la diffusion de documents scientifiques de niveau recherche, publiés ou non, émanant des établissements d'enseignement et de recherche français ou étrangers, des laboratoires publics ou privés.

1 **Incipient wolframite deposition at Panasqueira (Portugal): W-rutile and tourmaline**  
2 **compositions as proxies for the early fluid composition**

3

4 Eleonora Carocci<sup>a,\*</sup>, Christian Marignac<sup>a</sup>, Michel Cathelineau<sup>a</sup>, Laurent Truche<sup>b</sup>, Marc Poujol<sup>c</sup>,  
5 Marie-Christine Boiron<sup>a</sup>, Filipe Pinto<sup>d</sup>

6

7 <sup>a</sup> *Université de Lorraine, CNRS, GeoRessources, F-54500 Nancy, France*

8 <sup>b</sup> *Université de Grenoble Alpes, CNRS, ISTERRE, F-38041 Grenoble, France*

9 <sup>c</sup> *Université de Rennes, CNRS, Géosciences Rennes - UMR 6118, F-35000 Rennes, France*

10 <sup>d</sup> *Beralt Tin & Wolfram Portugal, 6225-051 Barroca Grande, Portugal & Instituto de Ciências da*  
11 *Terra, Rua Campo Alegre 687, 4169-007 Porto, Portugal*

12

13 Email: [eleonora.carocci@univ-lorraine.fr](mailto:eleonora.carocci@univ-lorraine.fr)

14

15

16 **Abstract**

17 The main event responsible for the deposition of tungsten at Panasqueira was closely associated  
18 with strong tourmalinization of the wall rocks. Tourmaline is coeval with a W-rich rutile (up to 8-10  
19 wt% W) and both minerals record an early introduction of W in the system, just before the main W  
20 deposition. Uranium-Pb dating of the rutile by LA-ICP-MS yielded an age of 305.2±5.7 Ma, which  
21 is 6-10 Ma older than the K-Ar age of 296.3±1.2 Ma obtained on muscovite, which was therefore  
22 not coeval of wolframite. Major and trace element concentration variations in tourmaline record  
23 fluid mixing between two end-members, both considered to be of metamorphic derivation on the  
24 basis of REE profiles. We report evidence for a fluid enriched in Co, Cu, Pb, Sc, Sr, V, Cr, Nb, Ta,  
25 Sn, interpreted to be of “local” origin, e.g., well-equilibrated with the host formations, and a fluid  
26 rich in Li, F, Fe, Mn, W inferred to be of deep origin and related to biotite dehydration. The second  
27 fluid carried the metals (in particular Fe and Mn) necessary for wolframite deposition, which were  
28 not necessarily inherited from the wall rocks through fluid-rock interaction. Micrometer scale  
29 variations in tourmaline and rutile crystal-chemistry are indicative of pulsatory fluid input during  
30 tourmalinization.

31

32

33

**Introduction**

34

35 Tungsten (W) in western Europe, was mainly concentrated during the Variscan orogeny. The  
36 total endowment is estimated to be 1.1 Mt W. The Central Iberian Zone (CIZ), which contains 210  
37 kt W, is one of the main provinces. Others include the Erzgebirge (270 kt W) and Cornwall ( $\geq 425$   
38 kt W) (Marignac and Cuney, 2013). The Panasqueira mine in the CIZ, which has been active for  
39 more than 130 years, exploits one of the largest W deposits in western Europe, with a total  
40 production of 76 kt W since 1934 and estimated total resources of  $\sim 38$  kt W (Almonty, 2016;  
41 Vigne et al., 2018), i.e., an *ab initio* endowment of at least 115 kt W.

42 Since the 1970s, numerous mineralogical, geochemical and fluid inclusion studies have  
43 discussed the genesis of the Panasqueira deposit (e.g., Kelly and Rye, 1979; Bussink, 1984; Snee et  
44 al., 1988; Polyá, 1989; Noronha et al., 1992; Lüders, 1996; Foxford et al., 2000; Polyá et al., 2000;  
45 Lecumberri-Sanchez et al., 2017; Codeço et al., 2017; Launay et al., 2018). The deposit, which is  
46 hosted by the Beira schists, and overlies an inferred contact with a granite pluton (inferred from the  
47 presence of a greisenized cupola), is characterized by thousands of sub-horizontal veins filled by  
48 wolframite and quartz. Following Kelly and Rye (1979), most studies have concluded that the  
49 granite intrusion played a major role in controlling a unique hydrothermal megacycle. Snee et al.  
50 (1988) dated muscovite at  $296.3 \pm 1.2$  Ma ( $2\sigma$ ), using the  $^{40}\text{Ar}/^{39}\text{Ar}$  age step-heating method, and  
51 considered this age to represent the approximate timing of the main W depositional stage, assuming  
52 coeval crystallization of wolframite and muscovite.

53 Recent investigations carried out on the scale of the whole deposit reported observations of  
54 mineral sequences synchronous with the incipient opening of the W veins. The fluid inclusion  
55 record of the event in which wolframite was deposited (the OSS stage of Polyá et al., 2000) was lost  
56 due to decrepitation and/or deformation after wolframite crystallization (Cathelineau et al., 2017;  
57 2018; Carocci, 2019), a fact which unfortunately was overlooked by all previous studies. As a  
58 result, there is no reliable record of the fluids responsible for wolframite crystallization. A potential  
59 way to constrain the composition of these early fluids is to study the crystal-chemistry and trace  
60 element concentrations in minerals coeval with incipient wolframite deposition. Here, we  
61 demonstrate that tourmaline in the wall rock, and associated rutile, were indeed coeval with  
62 wolframite deposition. Both minerals display chemical zoning, taken as proxy for the evolution of  
63 the fluid chemistry during their growth. Tourmaline is known to be highly stable under a wide range  
64 of physico-chemical conditions (van Hinsberg et al., 2011). Its complex structure inhibits  
65 significant element diffusion on available timescales (Hawthorne and Dirlam, 2011) and records  
66 changes in fluid chemistry at all stages of crystal growth (Marschall and Jiang, 2011; Sluck and  
67 Trumbull, 2011; van Hinsberg et al., 2011). Although several studies of the Panasqueira tourmaline  
68 have examined the major element and boron isotope composition (Neiva et al., 2007; Codeço et al.,

69 2017; Launay et al., 2018), none have investigated the trace element chemistry and the possibility  
70 that it could record the evolution of the fluid or change(s) in the fluid source(s).

71 The main objective of this study was therefore a comprehensive analysis of tourmaline and rutile  
72 chemistry in order to constrain the nature of the ore forming fluids. This resulted in a modified  
73 conceptual model of the early hydrothermal system at Panasqueira. A subordinate objective was to  
74 date the rutile using the *in situ* U-Pb method, in order to constrain the onset of hydrothermal activity  
75 and provide a comparison to the published  $^{40}\text{Ar}$  muscovite age.

76

77

### Regional background

78

79 Panasqueira is located in the Iberian Massif, which is the southern branch of the so-called  
80 Iberian-Armorican Arc (IAA), at the western termination of the Variscan belt. The IAA is an  
81 orocline formed in about 10 Ma at the end of the Carboniferous (Weil et al., 2013). The Iberian  
82 Massif is subdivided into a number of tectonostratigraphic units (or Zones) (Julivert et al., 1972)  
83 delimited by tectonic boundaries (Fig. 1). Most of these terranes are Gondwanian in origin. The  
84 Central Iberian Zone (CIZ) is the main unit of a series of autochthonous terranes derived from the  
85 Paleozoic Gondwanian passive margin. They were covered by a unique nappe stack (Galicia-Tras-  
86 os-Montes Zone and Ossa Morena Zone) (Pérez-Caceres et al., 2017). The CIZ comprises a thick  
87 sequence of late Ediacarian-Cambrian metasedimentary rocks (the Schist-Greywacke Complex, or  
88 Beira Group) overlain unconformably by the Early Ordovician Armorican Quartzite (Diez-  
89 Fernandez et al., 2013).

90 The tectono-thermal Variscan history of the CIZ, which begins in the Early Carboniferous and  
91 ends in the Early Permian, is subdivided into five events, D1 to D5 (Diez-Fernandez et al., 2016,  
92 and references therein; Diez-Fernandez and Pereira, 2017). The first event, D1 crustal thickening  
93 and stacking of the allochthon, was dated at *c.* 354-347 Ma (e.g., Rubio Pascual et al., 2013). The  
94 subsequent D2-D5 evolution was characterized by large-scale crustal melting, resulting from a  
95 combination of mid-crustal post-thickening heating and mantle-derived heat input at the base of the  
96 continental crust (Pereira et al., 2017). The D2 (*c.* 327-316 Ma) event recorded the first episode of  
97 heat input and mid-crustal melting, with the development of migmatite domes (Fig. 1) (e.g., Llana-  
98 Fúnez and Marcos, 2007; Diez Fernandez et al., 2012; Rubio-Pascual et al., 2013; Pereira et al.,  
99 2017). Associated mafic syn-migmatitic sills and sheet-like bodies of late-kinematic monzogranite  
100 and granodiorite (319-316 Ma) are widespread (e.g., Castro et al., 2003; Pereira et al., 2017). The  
101 D3 to D5 evolution corresponds to a protracted sequence of episodic intra-crustal transcurrent  
102 deformation, initiated at ca. 315-310 Ma by the development of km- to 10 km-sized NW-SE to N-S

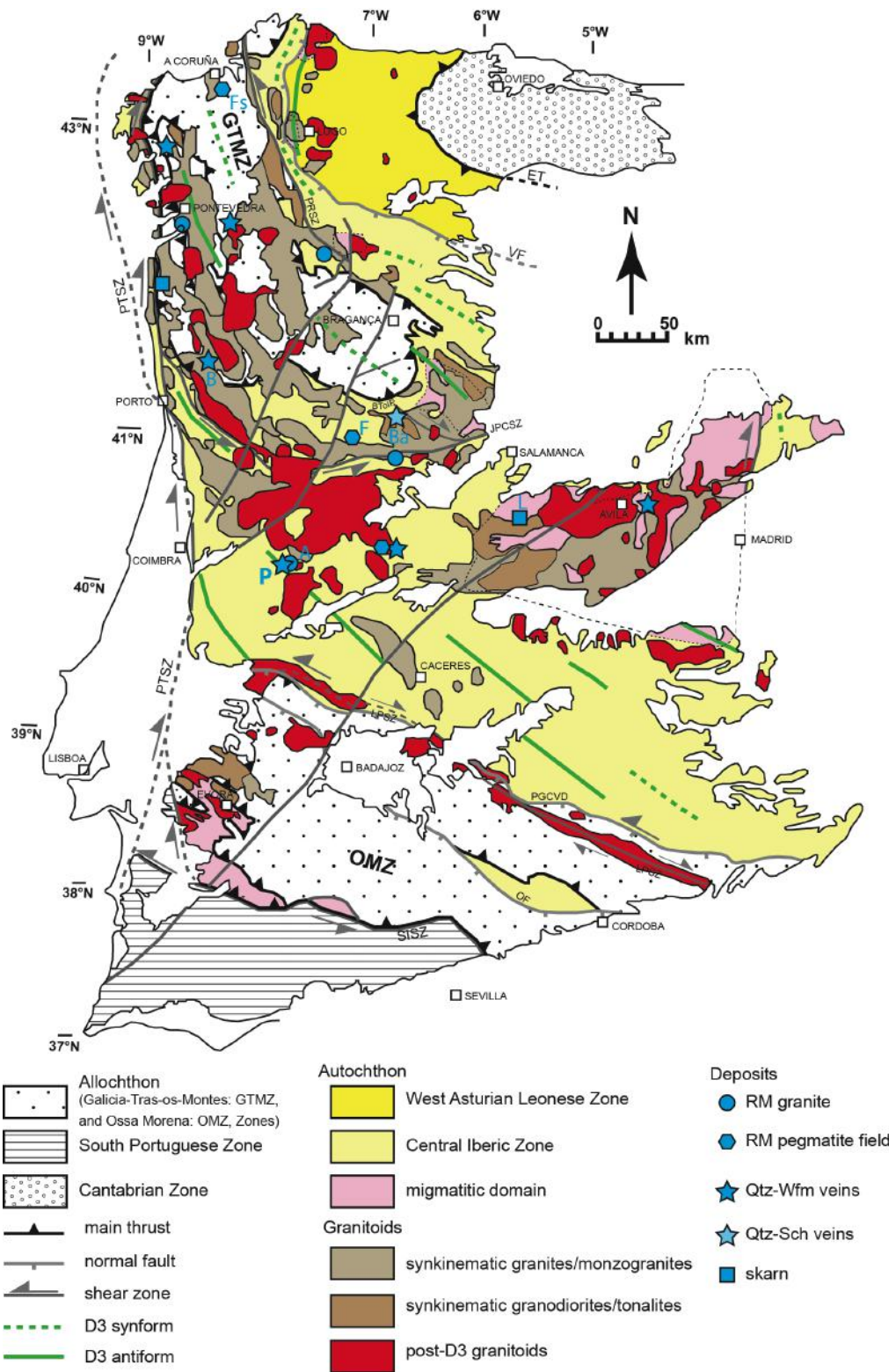


**Figure 1.** Geologic map of the Iberian Massif, with Panasqueira location. The map is adapted and simplified from Diez Fernandez et al. (2016), with complementary data from Alcock et al. (2015), Llana-Furez and Marcos (2007), Rubio Pascual et al. (2013) and Rubio-Pascual et al. (2016). BTtoIP: basal thrust of the Iberian Parautochthon; ET: Espina thrust, JPCSZ: D4 Jusbado-Perralva do Castelo shear zone; LPSZ: Los Pedroches shear zone; OF: Onza fault; PGCVD: Puente Genave-Castelo Vide detachment fault; PRSZ: Palas de Rei shear zone; PTSZ: Porto-Tomar D5 shear zone; SISZ: South Iberian shear zone; VF: Viveiro fault

110 upright F3 folds, with a S3 axial-plane schistosity, followed by D4 (*c.* 309-305 Ma) left-lateral and  
111 D5 (*c.* 304-295 Ma) dextral faulting (Diez Fernandez and Pereira, 2017; and references therein).  
112 Crustal melting and concomitant mantle-derived heat input continued through D3 to D5, with the  
113 pervasive emplacement of syn- to post-kinematic granite plutons, in three pulses roughly coincident  
114 with the D3 to D5 events (e.g., Dias et al., 1998; Mateus and Noronha, 2010; Sant'Ovaia et al.,  
115 2010; Fernandez-Suarez et al., 2011). Water-absent dehydration melting (incongruent biotite  
116 melting) produced cordierite-bearing diatexites in the cores of D2 migmatitic domes (Pereira  
117 Gomez et al., 2000). Permian mafic dikes (290-265 Ma) testify to a mantle influence until the very  
118 end of the collision (Orejana et al., 2009; Scarrow et al., 2011).

119 Numerous mineralized systems were active in the CIZ in close association with Late  
120 Carboniferous tectonics and granitoid emplacement giving rise to more than 150 peri- and intra-  
121 granitic rare metal (Nb-Ta, Li, W, Sn) and shear-zone hosted (Au-Ag-As-Sb-Pb-Zn-Cu) deposits  
122 (Tornos et al., 2000; Neiva, 2002; Mateus and Noronha, 2010; Noronha, 2017).

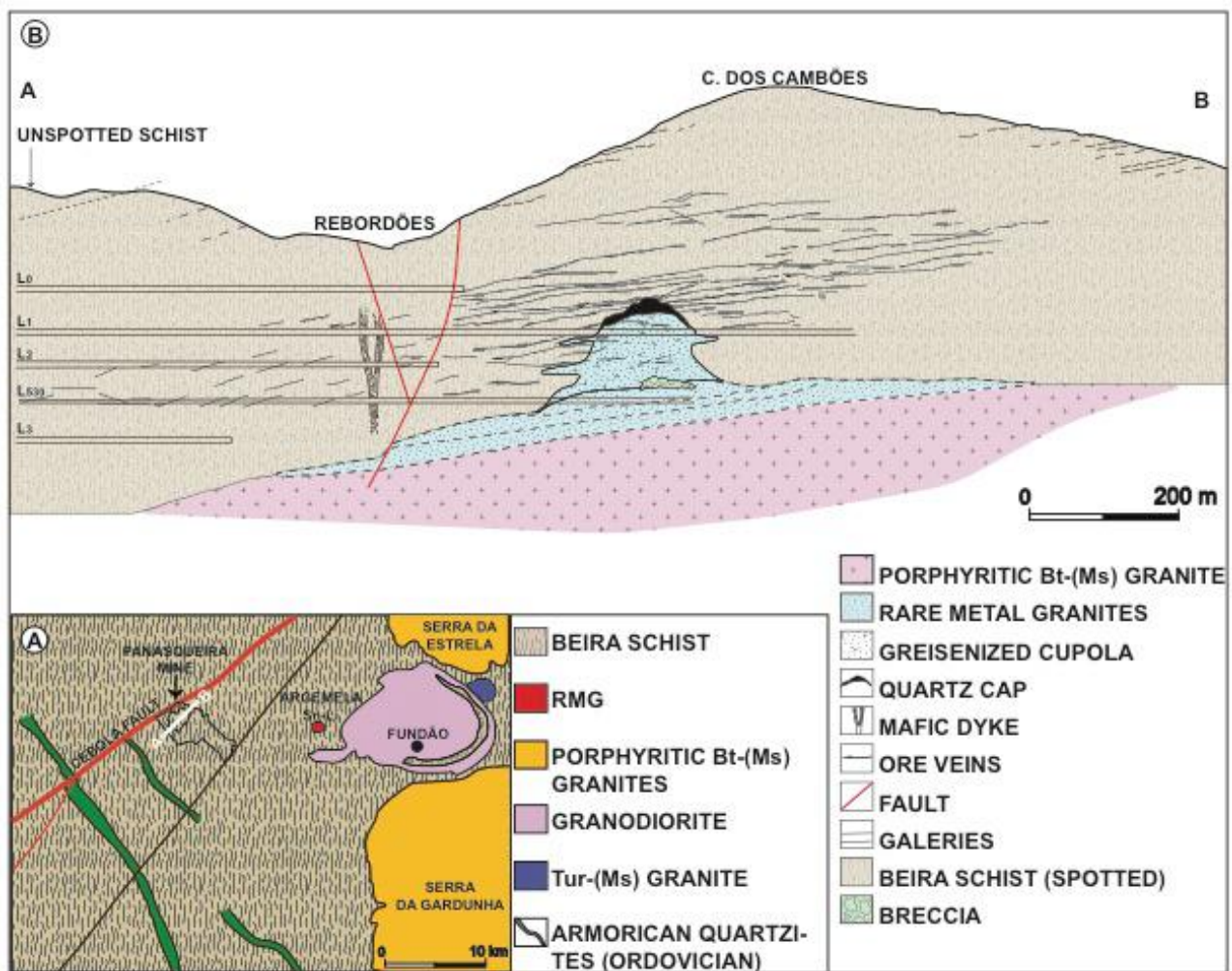
123

## 124 **Geological setting and previous work**

125

126 The Panasqueira W-Cu (Ag)-Sn deposit in central Portugal lies within the Central Iberian Zone  
127 (CIZ) (Fig.1), in the core of a late Carboniferous anticlinorium bordered by narrow synclines of  
128 Ordovician Armorican Quartzite (Fig. 2-A). The deposit consists of a dense network of sub-  
129 horizontal mineralized quartz veins crosscutting the subvertical foliation of the greenschist facies  
130 mica-schists of the Beira Schists (Fig. 2-B). These veins crosscut numerous pods and vein-like  
131 masses of barren quartz locally named “seixo-bravo” which are probably late kinematic and cover  
132 an area of over six km<sup>2</sup>; their vertical extent is several hundred meters (Polya, 1989).

133 A granite body concealed beneath the deposit (Fig. 2-B) was responsible for a 6x3 km  
134 metamorphic contact aureole of schists, marked by cordierite-biotite spots and cordierite-andalusite  
135 assemblages. These mineral assemblages constrain the pressure to have been less than 300 MPa at  
136 the time of emplacement of the Panasqueira granite (Pattison, 2001; Kuhn, 2018). A greisenized  
137 cupola at the top of the granite is still observed in some of the galleries. This cupola was described  
138 by Kelly and Rye (1979) as having being overlain by a quartz cap, although this has not been  
139 corroborated. The greisenized cupola sits atop a sheet-like body of evolved granites that are mainly  
140 evident in a few drill holes (Bussink, 1984; De Amorin, 2017), but have been encountered locally in  
141 some of the deepest galleries of the mine (LB level, Barroca Grande sector: Lourenço, 2002). The  
142 cupola sent out several sill-like apophyses, and towards its base, a matrix-supported breccia formed  
143 with large (up to 2 m) joint-bounded hornfels clasts (Kelly and Rye, 1979). The greisenized cupola



144  
 145 **Figure 2.** Panasqueira geological setting. A. Geologic map of the Panasqueira area (redrawn from Ribeiro, 2017),  
 146 with location of the cross section in B. Note the tight synform roots picked out by Ordovician quartzites. B. Cross  
 147 section of the Panasqueira deposit (adapted from Bussink, 1984 and De Amorin, 2017)  
 148

149 is cut by the quartz-wolframite veins. The evolved granites are typical of the peraluminous rare  
 150 metal granite (RMG) family (Linnen and Cuney, 2005), and are albite-rich, displaying typical  
 151 “snowball” quartz textures. They contain (rare) cassiterite and columbo-tantalite as accessory  
 152 minerals (Lourenço, 2002; De Amorin, 2017). A porphyritic (K-feldspar megacrysts) biotite-  
 153 (muscovite) granite (Bussink, 1984) is likely representative of the main granite body responsible for  
 154 the metamorphic aureole and could be related to the late D3 granites from the nearby Serra de  
 155 Estrela (Sant'Ovaia et al., 2010) and Serra de Gardunha (Fig. 2-A). According to recent gravimetric  
 156 data (Ribeiro, 2017), the main Panasqueira granite has the shape of a laccolith, with a flattened top,  
 157 a NNE striking elongated trend (~6.3×3.8 km) and an average thickness of 1 km, but with a 2 km  
 158 thick keel. The evolved granites have been dated at c. 290 Ma, by whole-rock K-Ar (Clark, 1970) or  
 159 Rb-Sr (Priem and Den Tex, 1984) methods. Close to the deposit, the Fundão granodiorite (Garcia,

160 2004) and the small Argemela RMG intrusion (Michaud et al., 2020) are associated with a quartz-  
161 cassiterite vein system (Inverno et al., 2009).

162 The Panasqueira deposit first attracted research attention in the second half of the 20<sup>th</sup> century  
163 (Kelly and Rye, 1979; Polya et al., 2000, and references therein; Lourenço, 2002; Burnard and  
164 Polya, 2004) and continues to be the subject of considerable interest. Jaques and Pascal (2017) and  
165 Jacques et al. (2018) addressed the tectonic and fluid pressure conditions required for the creation  
166 and opening of the quartz vein system. Lecumberri-Sanchez et al. (2017), using LA-ICP-MS  
167 analyses of fluid inclusions, and Codeço et al. (2017), using B-isotope data from tourmaline,  
168 addressed the origin of the fluids. Launay et al. (2018) used tourmaline growth features to interpret  
169 the direction and velocity of flow of the fluids.

170

171

172

### **Samples and methods**

173 Our work is based on analyses of >250 samples collected in the late 1970s on levels 0 and 1, in  
174 the historical centre of the mine, and in 2015-2016 on levels 0 to 3, to the south-west of the  
175 historical zones. Following petrographic examination with an OLYMPUS BX51 (transmitted and  
176 reflected light) optical microscope and a VHX-200 KEYENCE numeric microscope, selected  
177 samples were studied with a Schottky-FEG (Field Emission Gun) JEOL J7600F scanning electron  
178 microscope (SEM) equipped with an SDD-type EDS spectrometer at the GeoRessources Laboratory  
179 (Nancy, France). Backscattered electron (BSE) images were obtained after setting the acceleration  
180 voltage at 15 kV.

181 Major-element mineral compositions were determined for tourmaline and rutile using a  
182 CAMECA SX100 Electron microprobe (EPMA) equipped with a wavelength dispersive  
183 spectrometer (WDS) and a Schottky-FEG (Field Emission Gun) JEOL J7600F scanning electron  
184 microscope (SEM) equipped with a SDD-type EDS spectrometer at the GeoRessources Laboratory  
185 (Nancy, France). The analytical conditions were a 12 nA current and an accelerating voltage of 15  
186 kV for the EPMA, and a 1 nA current and an acceleration voltage of 15 kV for the SEM, with a  
187 counting time of 10 s. The same natural and synthetic oxides and silicate standards were used for  
188 the two types of analyses. For tourmaline analysis, these standards were topaz (F), albite (Na),  
189 olivine (Mg), orthoclase (Si, K), wollastonite (Ca), MnTiO<sub>3</sub> (Ti, Mn) and hematite (Fe). For rutile  
190 analysis, the standards were TiO<sub>2</sub> (Ti), Cr<sub>2</sub>O<sub>3</sub> (Cr), vanadinite (V), hematite (Fe), LiNbO<sub>3</sub> (Nb),  
191 LiTaO<sub>3</sub> (Ta), cassiterite (Sn) and scheelite (W).

192 Trace and rare earth elements in tourmaline were analyzed at the GeoRessources Laboratory,  
193 using a 193 nm GeoLas Pro ArF Excimer laser at 5 Hz laser frequency, the aerosols being analyzed

194 with an Agilent 7500c Quadrupole ICP-MS. The analytical settings for laser ablation are detailed in  
195 Leisen et al. (2012) and Lach et al. (2013). Laser ablations were performed with a constant fluence  
196 of  $10 \text{ mJ.cm}^{-2}$  and a constant repetition rate of 5 Hz. Helium was used as a carrier gas to transport  
197 the laser generated aerosols from the ablation cell to the ICP-MS. Before entering the ICP torch,  
198 Helium was mixed with Argon at a typical flow rate of  $0.5 \text{ l.min}^{-1}$ . The hole produced by the laser  
199 was  $24 \text{ }\mu\text{m}$  in diameter, except for REE measurements, for which it was  $120 \text{ }\mu\text{m}$  in diameter. A  
200 peak hopping ablation mode was initiated  $\sim 20 \text{ s}$  after the beginning of signal acquisition, in order  
201 to sample the background signal before ablation (used for data reduction), and was stopped after  
202 200 pulses. The return of the background signal to its initial value was checked before ablating a  
203 new zone. The NIST reference glasses 610/612 were used as external standards; Si, previously  
204 analysed by EPMA, was used as an internal reference. The data were processed using the Iolite  
205 software (Paton et al., 2011).

206 Rutile U-Pb geochronology was conducted by in-situ laser ablation ICP-MS at Géosciences  
207 Rennes using an ESI NWR193UC Excimer laser coupled to a quadrupole Agilent 7700x ICP-MS  
208 equipped with a dual pumping system to enhance sensitivity (Paquette et al., 2014). The  
209 instrumental conditions are reported in Appendix A1, Table A1. The ablated material was carried  
210 into helium, and mixed with nitrogen and argon, before injection into the plasma source. The  
211 instrument was aligned and calibrated for mass before each analytical session using the NIST SRM  
212 612 reference glass, by inspecting the  $^{238}\text{U}$  signal and minimizing the  $\text{ThO}^+/\text{Th}^+$  ratio ( $<0.5\%$ ).  
213 During the course of an analysis, signals for  $^{204}(\text{Pb}+\text{Hg})$ ,  $^{206}\text{Pb}$ ,  $^{207}\text{Pb}$ ,  $^{208}\text{Pb}$ ,  $^{232}\text{Th}$  and  $^{238}\text{U}$  masses  
214 were acquired.

215 Single analyses consisted of 20 s of background integration followed by 60 s of sample  
216 integration with the laser firing and then a minimum delay of 10 s to wash out the previous sample.  
217 Ablation spot diameters of  $45 \text{ }\mu\text{m}$  with repetition rates of 5 Hz were used for all the analyses. For  
218 each analytical session, we used the following standard bracketing procedure. Two analyses of the  
219 R10 rutile standard (Luvizotto et al., 2009) were used as the primary rutile reference, and one  
220 analysis of the R19 rutile standard ( $489.5 \pm 0.9 \text{ Ma}$ , Zack et al., 2011) was used for quality control,  
221 followed by six analyses of the rutile grains. This sequence was repeated three times with an  
222 analysis of the R19 standard and two analyses of the R10 standard at the end of the session.

223 The data were corrected for U-Pb fractionation and for mass bias by repeated measurements of  
224 the R10 rutile standard. The R19 rutile standard measurements, treated as unknowns, were used to  
225 control the reproducibility and accuracy of the corrections. These standards yielded an age of  $490 \pm$   
226  $3 \text{ Ma}$  (MSWD = 1.11;  $n=13$ ) during the April 2016 session and  $493 \pm 12 \text{ Ma}$  (MSWD=2;  $n=12$ )  
227 during the December 2017 session. The data reduction was carried out with the data reduction

228 scheme, VizualAge\_UcomPbine, a set of Iolite procedures that work with Igor Pro (Chew et al.  
229 2014). All the data were plotted at 2 sigma on Tera-Wasserburg Concordia diagrams using the  
230 Isoplot 3.75 software (Ludwig, 2012).

231 Analyses of  $^{40}\text{Ar}/^{39}\text{Ar}$  were performed at the University of Manitoba (Canada) using a multi-  
232 collector Thermo Fisher Scientific ARGUS VI mass spectrometer linked to a stainless steel Thermo  
233 Fisher Scientific extraction/purification line, a Photon Machines (55 W) Fusions 10.6 CO<sub>2</sub> laser,  
234 and a Photon Machines (Analyte Excite) 193 nm laser. Isotope abundances were corrected for  
235 extraction-line blanks, which were determined before every sample analysis. Line blanks in both the  
236 Excimer and CO<sub>2</sub> system averaged ~3 fA for mass 40 and ~0.013 fA for mass 36. Mass  
237 discrimination was monitored by online analysis of air pipettes based on a power law relationship  
238 (Renne et al., 2009), which gave  $D = 1.0081 \pm 0.0002$  per amu, based on 71 aliquots interspersed  
239 with the unknowns. A value of 295.5 was used for the atmospheric  $^{40}\text{Ar}/^{36}\text{Ar}$  ratio (Steiger and  
240 Jäger, 1977) for the purpose of routine measurement of mass spectrometer discrimination using air  
241 aliquots, and correction for atmospheric argon in the  $^{40}\text{Ar}/^{39}\text{Ar}$  age calculation. Corrections were  
242 made for neutron-induced  $^{40}\text{Ar}$  from potassium,  $^{39}\text{Ar}$  and  $^{36}\text{Ar}$  from calcium, and  $^{36}\text{Ar}$  from chlorine  
243 (Roddick, 1983; Renne et al., 1998; Renne and Norman, 2001). The data were plotted using  
244 DensityPlotter (Vermeesch, 2012). Complementary information is given in Appendix A2.

245

246

## Results

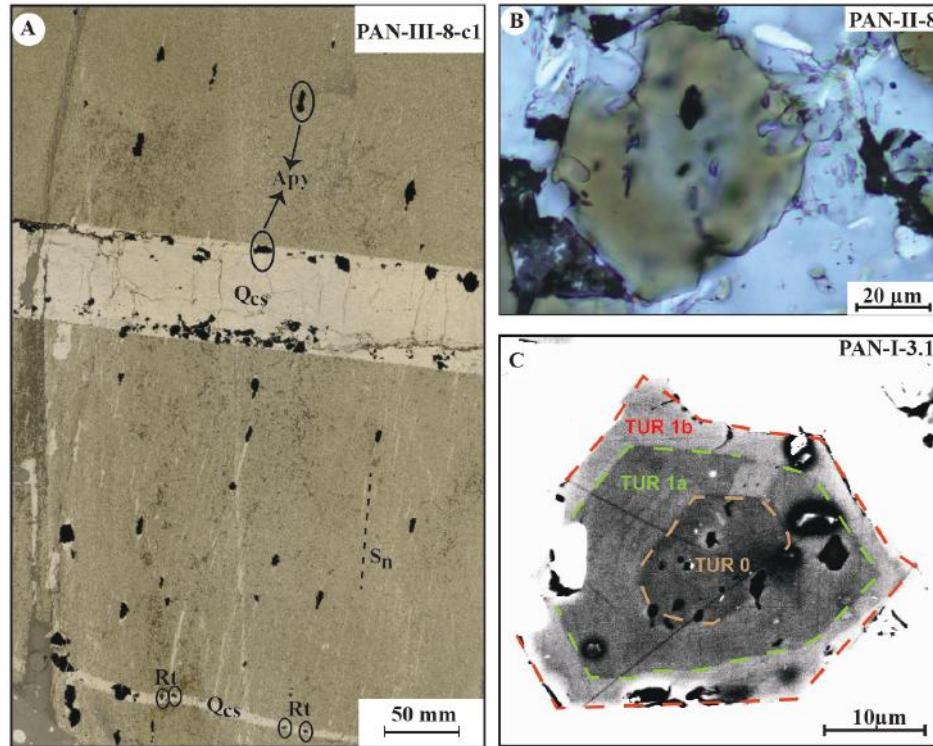
247

### *Petrography of the tourmalinized wall rocks*

248 *Petrography of the tourmalinized wall rocks*  
249 Tourmaline is a common mineral in the wall rocks to the W-veins in the Panasqueira deposit, but  
250 may also be observed far from the deposit, bordering either barren quartz veins or even “dry” joints.  
251 The tourmaline-bearing rocks extend from the vein/joint boundaries for distances varying from a  
252 few cm ( $\leq 10$ ) to 1 m, or roughly 25 cm on average.

253 As first noted by Bussink (1984), and later by Foxford et al. (1991), thin quartz veinlets (1-5 mm  
254 in average) are common in the tourmaline-bearing wall rocks adjacent to the main veins, and in  
255 many cases define the vein margins. They display clear evidence for a crack-seal mechanism of  
256 opening, and are labelled Qcs hereafter (Fig. 3-A).

257 There is a clear organization of the tourmaline in layers parallel to  $S_0$ , preserving the protolith  
258 fabric, as pointed out by Codeço et al. (2017). The tourmalinized wall rocks generally contain more  
259 than 50 vol.% tourmaline and tourmaline abundance is locally high enough to classify the rock as  
260 tourmalinite. Tourmaline is invariably associated with quartz, and with muscovite in the most  
261 pelitic protoliths, where the mica defines the schistosity. It is accompanied by abundant rutile (see



262

263 **Figure 3.** A. Typical tourmalinized wall-rock, with Qcs quartz veinlets. Sn, regional schistosity. Note the numerous  
 264 overprinting arsenopyrite (Apy) crystals. Sample PAN-III-8-c1 (NL). B. Poorly zoned tourmaline 1 seen in natural  
 265 light. Sample PAN-II-8. C. Typical zoning of tourmaline 1(BSE), showing the three Tur0, Tur1a and Tur1b zones.  
 266 Sample PAN-I-3-1.

267

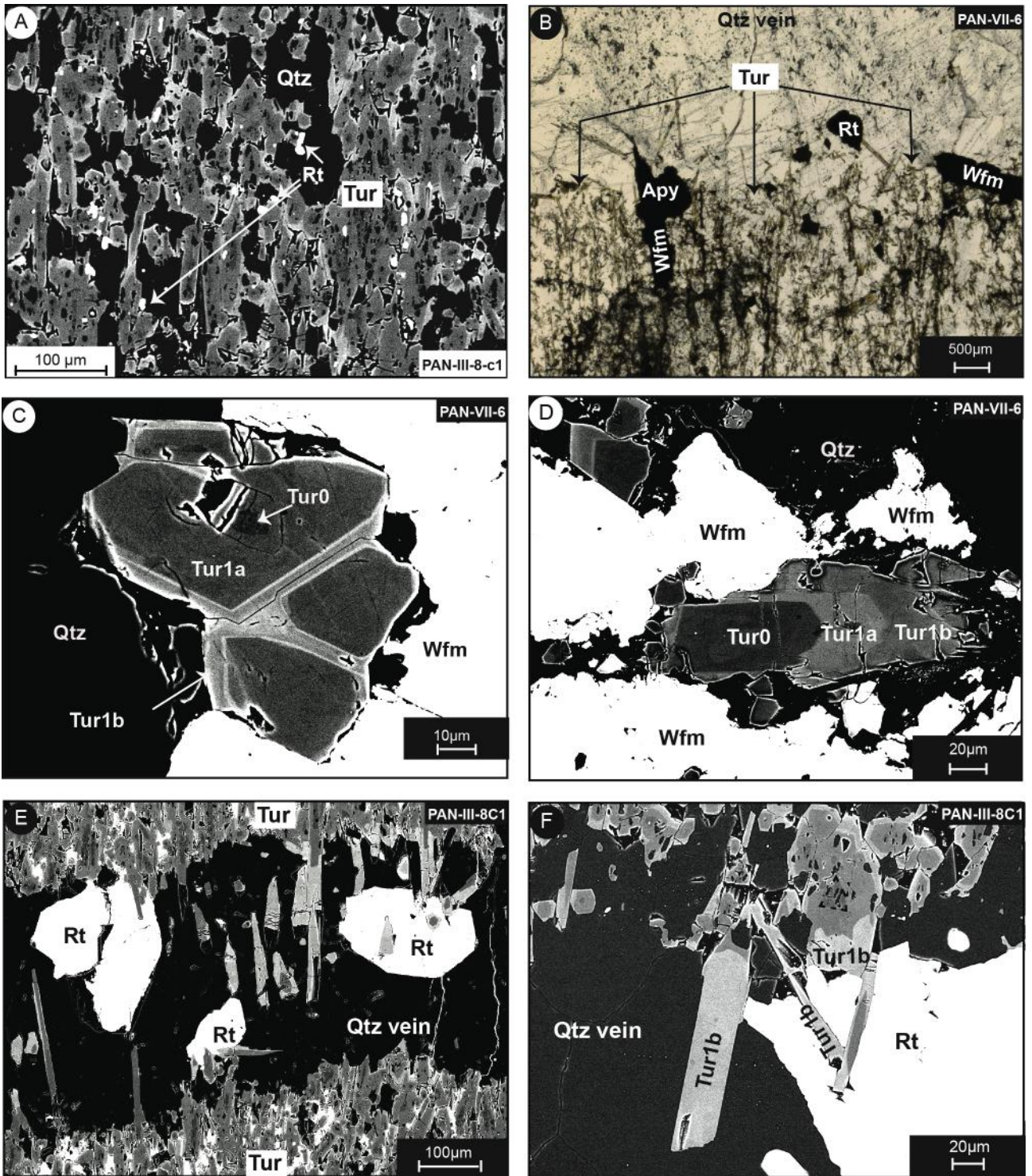
268 below), zircon and fluor-apatite and sporadic monazite or xenotime crystals, usually no more than  
 269 10-20  $\mu\text{m}$ , and commonly only a few  $\mu\text{m}$  in diameter. Aggregates of micrometer-scale crystals of  
 270 zircon and xenotime or zircon and monazite are common. In addition to these ubiquitous  
 271 accessories to the tourmaline, a number of other hydrothermal minerals were later involved in the  
 272 alteration of the Panasqueira wall rocks, and include quartz (silicification), topaz, muscovite,  
 273 sulfides (pyrrhotite, sphalerite, chalcopyrite, arsenopyrite), apatite and siderite.

274

### 275 ***Tourmaline textures***

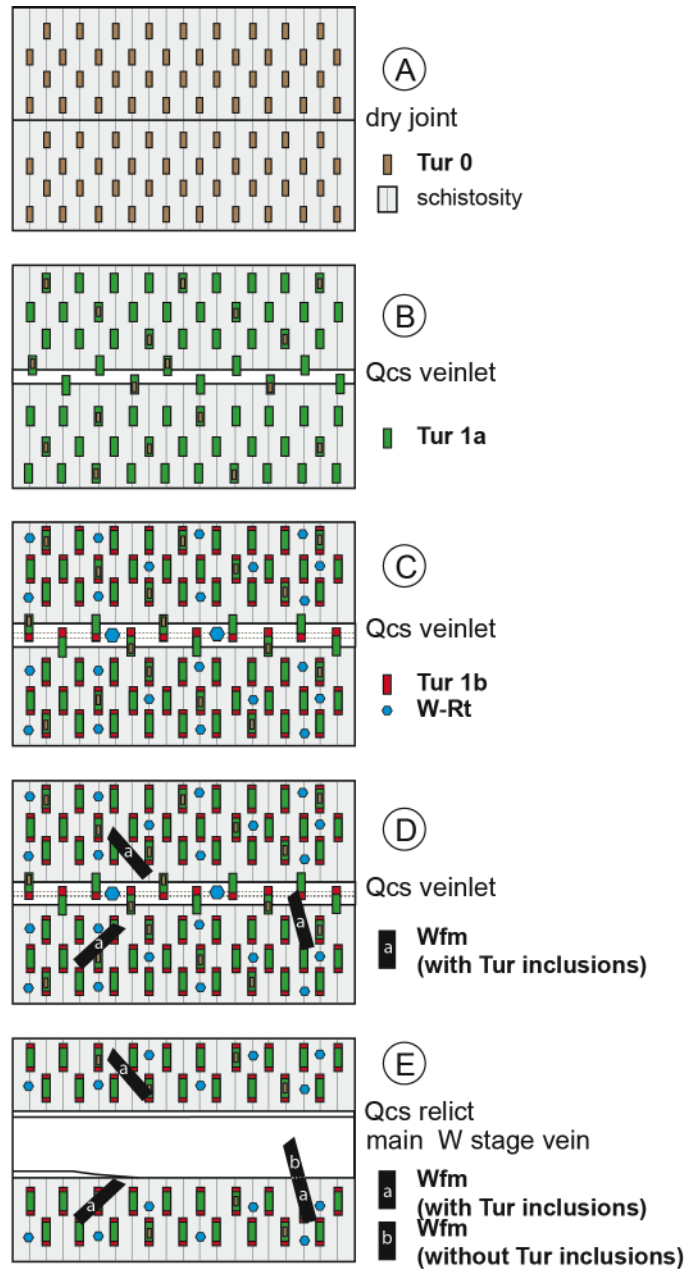
276 *Tourmaline habit and zoning:* The tourmaline habit may be either acicular, with lengths between  
 277 500  $\mu\text{m}$  and 1 mm and diameters of 20-50  $\mu\text{m}$ , or, more commonly, stocky prismatic, with lengths  
 278 between 50 and 150  $\mu\text{m}$  and diameters of 10-20  $\mu\text{m}$  (Fig. 4-A, B). The prisms are mostly sub-  
 279 parallel to the schistosity of the Beira schists (Fig. 4-A), but they may be perpendicular to it.  
 280 Contact metamorphic cordierite was replaced by tourmaline (Bloot and de Wolf, 1953).

281 The tourmaline crystals are brown and weakly zoned in thin section (Fig. 3-B), but display well-  
 282 characterized growth zoning in SEM images (Fig.3-C and 4-C, D) expressed as nearly homogenous



283  
 284 **Figure 4.** A. Typical early assemblage in the tourmalinized wall-rock, with Tur1 elongated along (erased) schistosity  
 285 and disseminated rutile. Sample PAN-III-8-c1 (SEM). B. Acicular tourmaline in a silicified wall-rock. Sample PAN-  
 286 VII-6-b1 (NL). C-D. Evidence for coeval growth of Tur1b and early wolframite: C. Wolframite growth inhibited the  
 287 development of Tur1b zones; D. Wolframite growth progressively inhibited first Tur1a, then Tur1b growth. Sample  
 288 PAN-VII-6-b1 (SEM). E-F. Evidence for coeval growth of Tur1b and the W-rich rutile in a Qcs veinlet. Sample PAN-  
 289 III-8-c1 (SEM).

291 zones of variable grey intensity, with sharp boundaries. A dark irregularly shaped core is commonly  
 292 present, although not systematically, but there is no evidence for sector zoning. These cores are  
 293 interpreted to be relicts of the early tourmaline and are labelled Tur0 hereafter. The outer parts of  
 294 the tourmaline prisms comprise a medium grey zone, labelled Tur1a and a clearer rim, labelled  
 295 Tur1b. In rare cases, there is an outermost rim characterized by the recurrence of a darker hue.



296  
 297 **Figure 5.** Synthesis of the stage Ia tourmalinization. **A.** Initialization of alteration (Tur0) in relation to simple “dry”  
 298 joints. **B.** Main tourmaline development (Tur1a) and first increments of opening in Qcs veinlets. **C.** Growth of Tur1b  
 299 tourmaline relative to increments of Qcs opening and coeval rutile growth. **D.** Local variant with early wolframite  
 300 growing in the wall-rock coevally with Tur1b. **E.** Transition to the main wolframite deposition stage

301  
 302 Some changes in the relative proportions of the different zones may be observed in relation to the  
 303 distance from the vein boundaries. Distal to veins, the proportion of Tur0 zones is higher, on

304 average these zones are wider, locally the crystals display regular (prismatic) shapes and the  
305 development of Tur1b rims is less pronounced. Furthest from the veins, the Tur1b rim may even be  
306 absent. Close to the veins, there is a greater development of the Tur1b zone, and the Tur0 cores are  
307 less common, corroded, and tend to represent a comparatively smaller proportion of the crystal  
308 volume. On the basis of a limited number of examples, it would appear that this tendency is roughly  
309 correlated with the presence of abundant wolframite in the nearby vein. Indeed, in the wall rocks of  
310 barren quartz veins, either in outcrop, or in the deeper levels of the mine (L3), Tur1b is usually  
311 absent.

312 Micro-inclusions are common in the tourmaline, although not systematically distributed. In order  
313 of importance, they are: zircon, rutile, quartz, and rare monazite, pyrite, and apatite. Most  
314 commonly, the inclusions “overprint” the zone boundaries, and in most cases, the proportion of  
315 inclusions is the same in the Tur1a or Tur1b zones. The Tur0 cores are relatively free of inclusions,  
316 except for those of quartz. The zircon may be zoned in respect to their U-Th content. In addition,  
317 microanalysis revealed the probable presence of concealed micro-inclusions (see below).

318 *Tourmaline and Qcs quartz veinlets:* Tourmaline prisms are systematically present at the walls  
319 of the Qcs veinlets, displaying both Tur1a and Tur1b zones, the latter usually developed to a far  
320 higher extent than in the wall rocks (Fig.4-E, F). Thus, as pointed out by Foxford et al. (1991), the  
321 development of both the main Tur1a tourmaline prisms and the Tur1b rims was coeval with the first  
322 increments of vein opening evident by the Qcs veinlets. This is pictured schematically in Fig. 5. The  
323 very existence of Tur0, which is typically absent from the Qcs veinlets, nonetheless demonstrates  
324 that the onset of tourmalinization was earlier than these veinlets (stage A in Fig. 5).

325 *Tourmaline and other alteration minerals:* Irrespective of the nature and the number of  
326 hydrothermal minerals in the wall rocks, the tourmaline crystals invariably display the same  
327 sequence of Tur0-Tur1a-Tur1b crystallization. Other alteration minerals are typically later. For  
328 example, the occurrence of topaz and/or muscovite is accompanied by a distinct overgrowth on  
329 Tur1b rims. In the same way, the development of apatite-bearing vugs in the tourmalinized wall  
330 rocks was accompanied by distinct overgrowths on the undissolved tourmaline crystals. As sulfides  
331 (chalcopyrite, sphalerite, pyrrhotite) and siderite are mainly present as stringers in the wall rocks, it  
332 is easy to recognize that these stringers overprint tourmaline 1 prisms and their characteristic  
333 zoning.

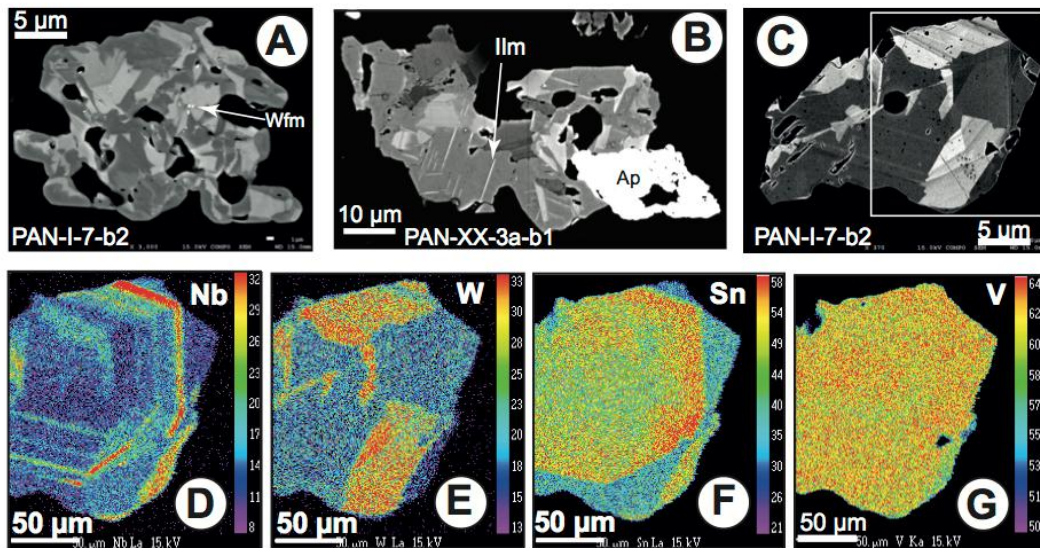
334 Small euhedral arsenopyrite crystals, a few 100  $\mu\text{m}$  in diameter, are frequently disseminated in  
335 the wall rocks (Fig. 3-A), locally (but not commonly) with inclusions of zoned tourmaline prisms.  
336 Nevertheless, arsenopyrite grew after the Tur0-Tur1a-Tur1b sequence, because: (i) arsenopyrite  
337 mostly replaced tourmaline prisms, and (ii) arsenopyrite overprinted Qcs veinlets (Fig. 3-A).

338 *Tourmaline and wolframite*: Wolframite from the mineralized veins is not, as a rule, associated  
339 with tourmaline but developed as large crystals along the walls of the open fractures. There are rare  
340 occurrences of the development of wolframite crystals in the wall rock, close to the mineralized  
341 veins (Fig. 4-B). These crystals include zoned tourmaline, and detailed observations show that  
342 wolframite growth was either coeval with Tur1b rim development or slightly later (Fig.4-C, D).  
343 This wolframite was, in turn, reworked in relation to the main opening and deposition of the main  
344 wolframite, which is consistently devoid of any tourmaline inclusions (stages E and F in Fig. 5).

345

### 346 *Rutile textures*

347 Rutile is systematically associated with tourmaline, being present both in the wall rocks, as small  
348 (from 10  $\mu\text{m}$  to 80-100  $\mu\text{m}$ ) crystals, scattered or densely disseminated, or as large (up to 500  $\mu\text{m}$  or  
349 more) isolated crystals in the Qcs veinlets, where they were clearly coeval with Tur1b growth (Fig.  
350 4-E, F). Micro- to nano-inclusions (from about 1  $\mu\text{m}$ , to <100 nm) of wolframite are common. They  
351 are usually located at crystallographic boundaries (e.g., faces intersections, twin planes, quartz  
352 inclusion boundaries) showing that they were coeval with the host rutile (Fig. 6-A). Their  
353 compositions, estimated from SEM-EDS measurements, are ferberitic, with Fe/Fe+Mn ratios  
354 between 0.67 and 0.83.



355

356 **Figure 6.** Panasqueira rutile. A, B, C: Back-scattered SEM images. of Panasqueira rutile. A. Crystal aggregate from  
357 the wall-rock of a wolframite-bearing vein. Note the primary wolframite nano-inclusions (Wfm). B. Crystal in the wall  
358 rock of a barren vein from the deep L3 level. Note the ilmenite lamellae (Ilm) and the late apatite (Ap), overprinting the  
359 rutile crystal. C. Large isometric crystal from a Qcs vein in the wall-rock of a wolframite-bearing vein. Note the  
360 superimposition of sector zoning (SZ) on the compositional (oscillatory) zoning. Square: location of images D to G. **D**  
361 **to G:** false-color X-ray (EPMA) images, showing the differential effect of SZ on the minor element concentrations, and  
362 the anti-correlation of W and Nb in the OZ.

363 In the barren wall rocks, rutile crystals are less abundant and are characterized by the presence of  
364 inclusions of ilmenite lamellae (Fig. 6-B).

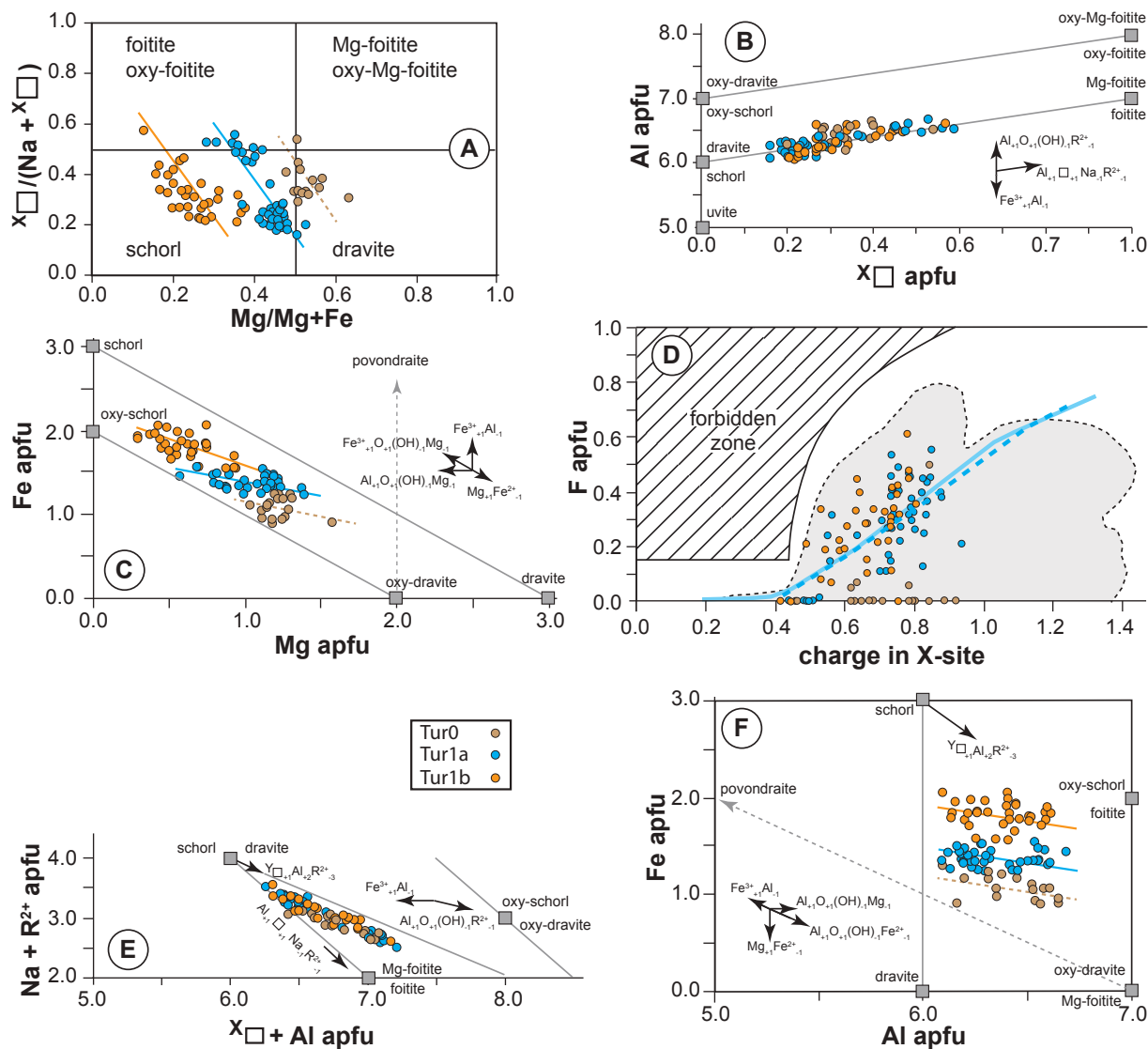
365

### 366 ***Tourmaline chemical composition***

367 *Major element crystal chemistry:* For reasons made explicit in Appendix A0, most analyses were  
368 performed using SEM-EDS. A total of 86 crystals from 19 representative samples was analyzed  
369 (Appendix A3: Table A3). No systematic variation in the compositions of the different zones was  
370 evident, however, either as a function of the distance to the vein boundary, or among tourmaline  
371 crystals from different settings (wall rock, Qcs veinlet, inclusions in early wolframite).

372 The structural formulae were calculated by normalizing to 26.5 (O, OH, F), which (with the  
373 assumption of stoichiometric boron) allowed us to take into consideration the fluorine content and  
374 not assume the filling of the Y site, which may contain Li, and possibly vacancies (Bosi, 2018). The  
375 generalized structural formula of the tourmaline super-group is  $XY_3Z_6(T_6O_{18})(BO_3)_3V_3W$  (Bosi,  
376 2018). The T site is occupied primarily by Si, which may be replaced by minor Ti, Al or B. The  
377 nine-coordinated site X may be occupied by  $Na^+$  and  $Ca^{2+}$ , or minor  $K^+$ , and vacancies ( $^X\Box$ ) may be  
378 present. This defines the main chemical groups of tourmaline: alkali, calcic and alkali-deficient  
379 groups (Henry et al. 2011). The V, or (O)3, site is occupied mainly by OH (and possibly O),  
380 whereas the W, or (O)1, site is occupied by OH, F or O, defining the hydroxy, fluor, and oxy  
381 groups, depending on the dominant anion in the site. The six-coordinated Z site is mainly occupied  
382 by trivalent cations (mainly,  $Al^{3+}$ , but also  $Fe^{3+}$ ,  $Cr^{3+}$ ), but may contain divalent cations, mainly Mg  
383 (Bosi, 2018). The six-coordinated Y site is occupied by mono- ( $Li^+$ ), bi- ( $Mg^{2+}$ ,  $Fe^{2+}$ ,  $Mn^{2+}$ ) and tri-  
384 valent (mainly  $Al^{3+}$ , and possibly  $Fe^{3+}$ ,  $Cr^{3+}$ ) cations, but vacancies ( $^Y\Box$ ) may also be present (Bosi,  
385 2018). Following the criteria of Henry and Dutrow (2011), calculated tourmaline formula were  
386 rejected if Si was  $> 6.15$  atoms per formula unit (*apfu*), the sum of the Y + Z + T cations was  $>15.5$   
387 *apfu*, or the sum of the X-site cations exceeded 1.1 *apfu*. For reasons given in Appendix A0, all  
388 analyses yielding Si *apfu* values  $> 6.12$  were rejected. Using the empirical formula of Bosi (2018),  
389 the  $^ZAl$  *apfu* content of the Z site was found to be relatively constant,  $\sim 5.23$  *apfu*, irrespective of the  
390 zone, and, whereas there was sufficient Mg to fill this site in Tur0 and Tur1a, a small  
391 complementary content of  $^ZFe$  was necessary in Tur1b (Table A3, Appendix A3).

392 Based on the classification diagram of Henry et al. (2011), which compares the normalized X-  
393 vacancy to the Mg# ( $Mg/(Mg+Fe)$ ) ratio, the tourmaline classifies mainly as schorl (Fig. 7-A). There  
394 is a systematic shift from Mg-rich (ferro-dravite) to Fe-rich compositions for the sequence Tur0 to  
395 Tur1a to Tur1b, and a tendency towards foitite compositions. Indeed, as shown in Figure 7-B, the  
396 X-site vacancy is between  $\sim 0.2$  and  $\sim 0.6$  *pfu* (and thus, the Panasqueira tourmaline trends toward



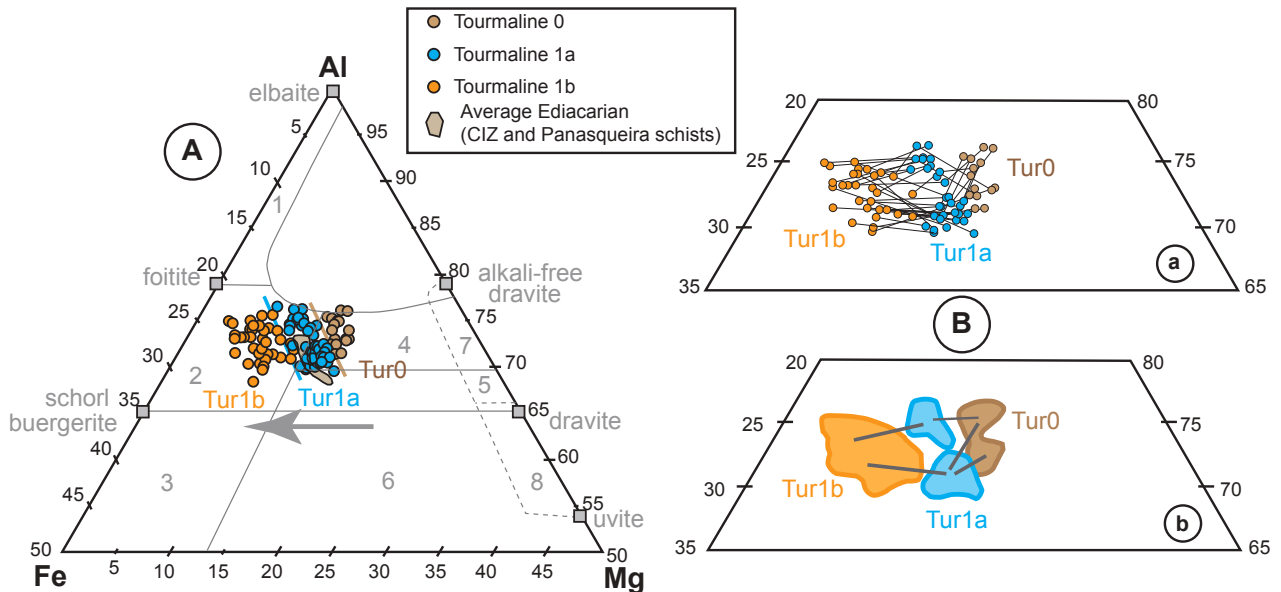
397

398 **Figure 7.** Crystal chemistry of the Panasqueira tourmaline, illustrating the characteristics of the Tur0, Tur1a and  
 399 Tur1b zones. Note in all the diagrams the continuity of composition variations among the three zones. **A.** Classification  
 400 diagram. **B.** Al vs. X-site lacune diagram, demonstrating the presence of a foitite component. **C.** Fe vs. Mg diagram,  
 401 illustrating the presence of an oxy-schorl component, together with the classical schorl-dravite exchange vector. **D.**  
 402 Linear relationships between F and the X-site charge; the forbidden zone and references are from Henry and Dutrow  
 403 (2011): grey domain, worldwide tourmaline (~ 8,900 values); light blue line: Cruzeiro gold mine fibrous tourmaline;  
 404 dashed blue line: McCombe pegmatite tourmaline (magmatic trend). **E.** Na + R<sup>2+</sup> vs. Al+X-site lacune diagram,  
 405 illustrating the deviation from the schorl (dravite)-foitite (Mg-foitite) exchange line due to a combination of the oxy-  
 406 schorl (dravite) exchange vector and a vector responsible for the creation of Y-site vacancy. **F.** Fe vs. Al diagram,  
 407 showing the combination of all exchange vectors involved in the Panasqueira tourmaline.

408

409 alkali-deficient species) corresponding to the operation of the  $Al_{+1}X_{+1}Na_{-1}R^{2+}_{-1}$  vector, which leads  
 410 to a solid solution between schorl-dravite and foitite-Mg-foitite. From Figure 7-C, E and G, it is  
 411 evident that other vectors combined to displace the observed trends from the preceding trend. The  
 412  $Al_{+1}O_{+1}(OH)_{-1}(Mg, Fe)_{-1}$  vector seems to have been particularly important, implying an oxy-schorl

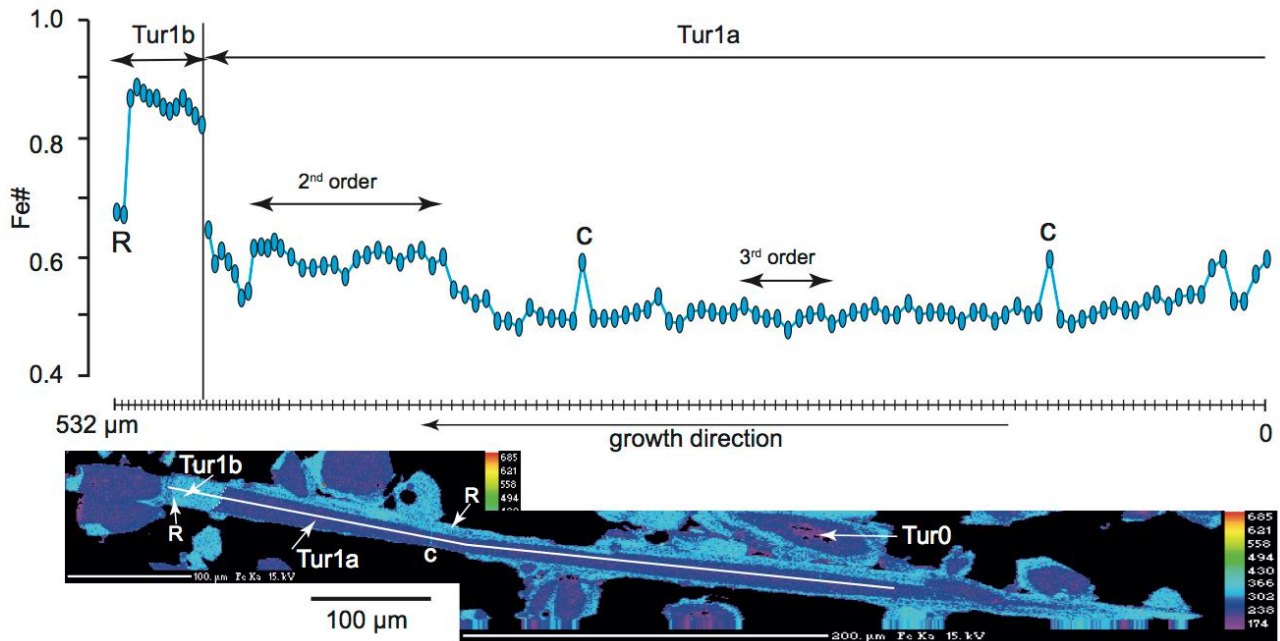
413 (or oxy-dravite) component, but the intervention of another exchange vector  $Y_{\square+1}Al_{+2}R^{2+}_{-3}$ ,  
 414 responsible for an Y-site vacancy (Bosi, 2011), seems to have been equally important. Indeed, a Y-  
 415 site vacancy is observed in our analyses, commonly larger than 0.1 *apfu*, and also those of Codeço  
 416 et al. (2017) and Launay et al. (2018) (Table 3, Appendix 3). This vacancy cannot be due to ignored  
 417 Li, because the LA-ICP-MS results (see below) show that the Li content is negligible, being at most  
 418 of ~330 ppm and averaging ~170 ppm (Tur1a) or ~290 ppm (Tur 1b); these contents would be  
 419 reflected by an amount of no more than 0.05 *apfu* Li and more commonly 0.02-0.04 *apfu*.



420  
 421 **Figure 8.** A. AFM diagram for the Panasqueira tourmaline, with location of the main tourmaline end-members. (1)-  
 422 (8) reference fields from Henry and Guidotti (1985): (1) Li-rich granitoids, (2) Li-poor granitoids, (3) Fe<sup>3+</sup>-rich quartz-  
 423 tourmaline rocks (hydrothermally altered granites), (4) Al-buffered metapelites, (5) not Al-buffered metapelites, (6)  
 424 Fe<sup>3+</sup>-rich quartz-tourmaline rocks, calc-silicate rocks, and metapelites, (7) low-Ca meta-ultramafics and Cr,V-rich  
 425 metasediments, and (8) metacarbonates and meta-pyroxenites. Compositions of CIZ schists from Oosterom et al. (1984)  
 426 and De Amorin (2017). The grey arrow emphasizes the global increase in Fe/Fe+Mg ratio from Tur0 to Tur1b. **B.**  
 427 Enlargement of A, illustrating the sequence Tur0-Tur1a-Tur1b: (a) individual paths, (b) synthesis. Note that, if there is a  
 428 jump from a zone to another, the starting and final compositions differ for each individual crystal.

429  
 430 In contrast to Tur0, which appears to be essentially free of fluorine, there is a distinct and similar  
 431 fluorine enrichment (up to ~1% F) of Tur1a and Tur1B, and a trend of increasing F *apfu* with X-site  
 432 charge (Fig.7-D). The latter is due to the high X-site Na content; Tur1a and Tur1b are Ca-poor,  
 433 whereas Tur0 is enriched in Ca, which, in turn, explains the higher X-site charge of Tur0 in Figure  
 434 7-D.

435 The complex covariations between aluminum, iron and magnesium that are depicted in Figure 7  
 436 are conveniently summarized in the AFM diagram of Figure 8-A, in which it is also possible to  
 437 identify the most common compositional paths from Tur0 to Tur1a and then Tur1b at the crystal



438

439 **Figure 9.** Profile of the Fe# ratio (Fe/Fe+Mg) along an acicular prism of tourmaline 1 (EPMA analyses), compared to  
 440 the false color X-image of the same crystal (sample PAN-VII-6-b2). The height of the elliptical symbol corresponds to  
 441 the estimated error on Fe#. Of the three zones (Tur0, Tur1a, Tur1b) seen on the X-image, only the two latter are  
 442 documented in the profile. At the rim of Tur1b zone, a recurrence of low Fe# is observed ®. Note the second and third  
 443 order modulations of the Fe# ratio along the profile. c: microcrack filled by Tur1b.

444

445 scale (Fig. 8-B). This figure illustrates an apparently continuous variation of the Fe to Fe+Mg ratio  
 446 (Fe#) from Tur0 to Tur1b, although detailed profiles show that there were small-scale modulations  
 447 of the Fe# during crystal growth (Fig. 9).

448 *Trace element contents:* As LA-ICP-MS analyses produce laser pits with a diameter of at least  
 449 24 μm, analysis to the desired detection limits was possible only for the largest Tur1 zones in a  
 450 limited number of crystals. Moreover, the tourmaline cores (Tur0) were too small for them to be  
 451 reliably analyzed, so analyses were restricted to the two external rims, Tur1a and Tur1b. A total of  
 452 77 spots, in 47 crystals from 7 samples were analyzed for their trace element concentrations. The  
 453 REE concentrations were also analyzed, but to obtain the required signal, a laser beam diameter of  
 454 120 μm was necessary, and therefore only two crystals, from two samples, could be analyzed for  
 455 the REE. This yielded an average composition of Tur1a and Tur1b zones from the two crystals. The  
 456 results are summarized in Table 1 and detailed in Appendix A4 (Table A4).

457 For some elements, several LA-ICP-MS spectra displayed anomalous peaks (anomalous values  
 458 in Table A4), interpreted as recording the presence of concealed micro- to nano-inclusions. Thus, a  
 459 Mn outlier at 2,600 ppm was likely due to siderite, and a Zn outlier at 8,500 ppm is interpreted to be  
 460 due to sphalerite. Several W anomalies record the presence of W-bearing minerals: W-bearing  
 461 rutile, where correlated with both Ti and Nb-Ta-Sn anomalies; cuprotungstite, where correlated

	Tur1a			Tur1b			detectio level
	min	max	average	min	max	average	
<b>Li</b>	26	170	72	48	288	130	
<b>Be</b>	1	21	8	0,8	21	4	
<b>Sc</b>	5	32	17	7	26	12	2
<b>Ti</b>	530	4360	1753	849	2840	1714	
<b>V</b>	37	613	341	11	742	282	
<b>Cr</b>	4	1027	271	9	601	156	8
<b>Mn</b>	135	528	421	310	606	468	20
<b>Co</b>	<i>0.2</i>	13	2	<i>0.2</i>	3	1	0.3
<b>Ni</b>	3	56	16	<i>0.2</i>	23	7	0.3
<b>Cu</b>	<i>0.3</i>	12	2	<i>0.3</i>	23	1	0.5
<b>Zn</b>	237	856	631	161	925	656	
<b>Sr</b>	10	285	79	7	131	40	
<b>Y</b>	<i>0.2</i>	7	1.4	<i>0.2</i>	5	0.9	0.3
<b>Nb</b>	<i>0.2</i>	12	0.6	<i>0.2</i>	2	0.2	0.3
<b>Ta</b>	<i>0.2</i>	0.5	0.2	<i>0.2</i>	0.2	0.2	0.3
<b>Sn</b>	4	54	24	4	157	19	3
<b>W</b>	<i>0.2</i>	29	4	<i>0.2</i>	21	3	0.4
<b>Pb</b>	2	33	6	1	15	4	

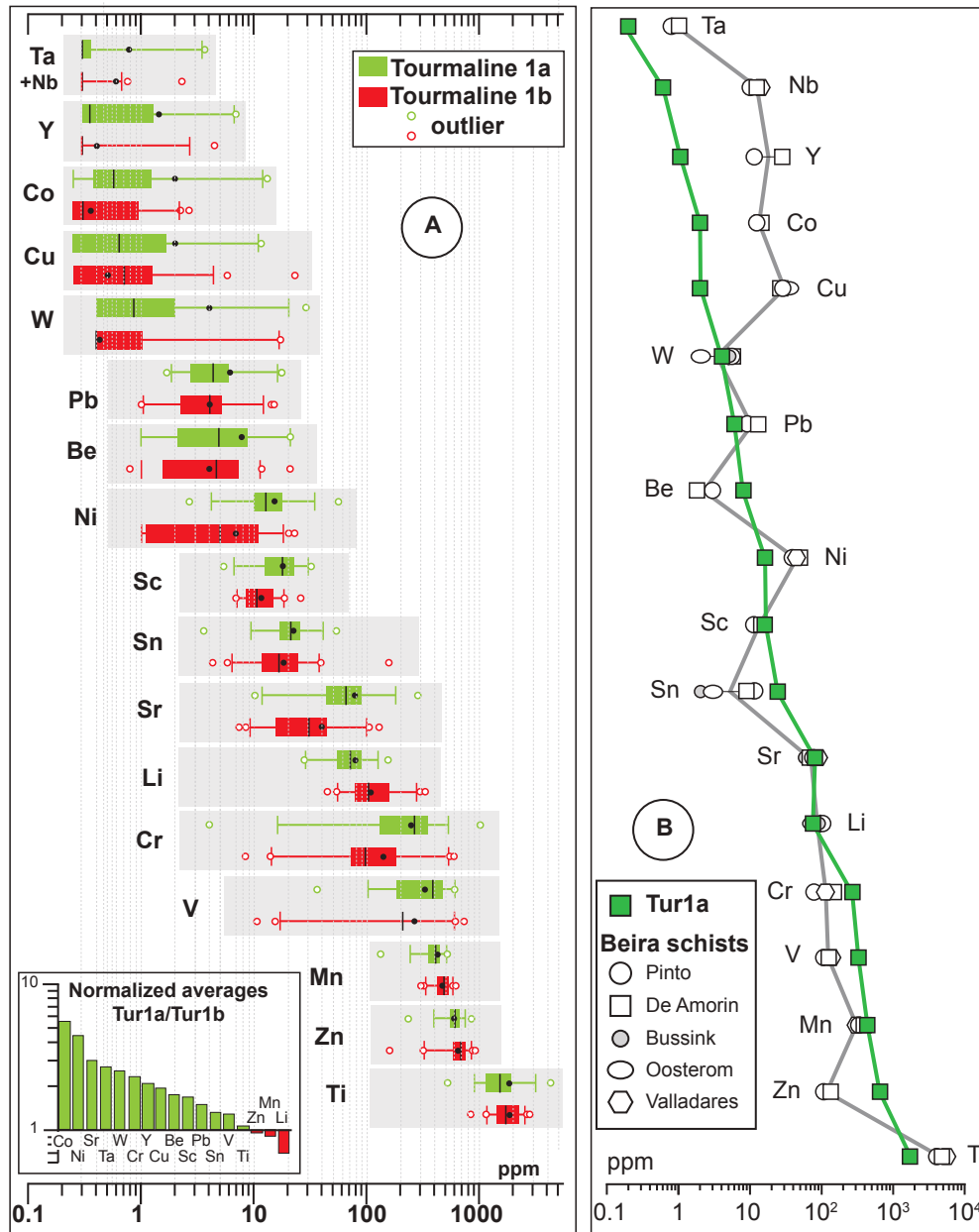
462 **Table 1.** Summary of LA-ICP-MS trace element analyses for the Panasqueira tourmalines. All contents in ppm. For  
463 the purpose of average calculations, the bdl (below detection level) in Table A4 were taken at half the detection level  
464 values (i.e., the without bias best estimates) when needed (italics). As a result, the averages for Nb (0.2 ppm) and Ta  
465 (0.2 ppm) are not provided in the table.

466

467 with a Cu anomaly (a rare occurrence); and wolframite, where no correlation was observed with  
468 either Ti or Cu. Most of these W anomalies were found in the Tur1b zones.

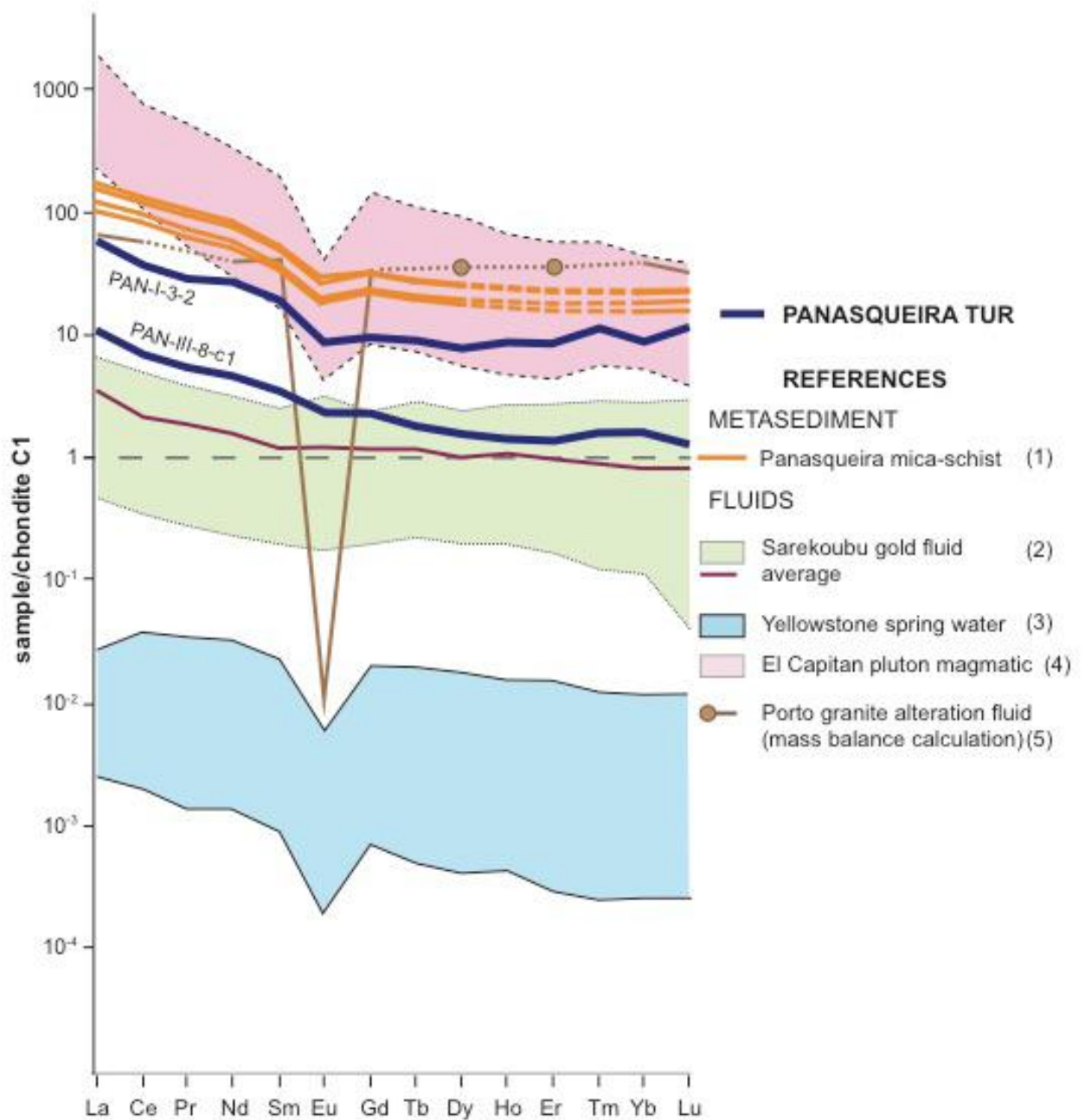
469 The results of the trace element analyses are illustrated in Figure 10-A (trace elements except  
470 REE) and Figure 11 (REE profiles). As seen in Figure 10-A, Ti, (530 to 4,360 ppm), Zn (160 to 930  
471 ppm) and Mn (135 to 600 ppm) are the most abundant trace elements, followed by Li (40 to 330  
472 ppm), V (10 to 740 ppm) and Cr (10 to 1,000 ppm). Strontium (7 to 285 ppm) and Sn (4 to 160  
473 ppm), are present in lower concentrations, followed by Sc (5 to 30 ppm), Be (3 to 20 ppm), and Pb  
474 (1 to 18 ppm). Concentrations of other elements were commonly below the detection level (*bdl*),  
475 e.g., Ni (up to 56 ppm), Co (up to 13 ppm) and Y (up to 7 ppm). Most measured tungsten  
476 concentrations were between 0.4 and 30 ppm, but for ~25 % of analyses of Tur1a and 50 % of  
477 Tur1b, the W concentration was below the detection level of 0.4 ppm. The measured concentrations  
478 for Nb are between 0.1 and 3.2 ppm, but for ~ 75% of the analyses, they were below the detection  
479 level of 0.3 ppm; the few measured Ta values were between 0.3 and 1.6 ppm; the overwhelming  
480 majority of analyses yielded values below the detection level of 0.3 ppm. From the limited REE  
481 data, the  $\Sigma$ REE concentration is low (between 1.2 and 12 ppm), and the REE profiles are

482 characterized by high  $La_N$  to  $Yb_N$  ratios of 6.37 to 6.77, and slightly negative  $Eu_N/Eu^*_N$  anomalies  
 483 (0.65 to 0.83) (Fig. 11).



484  
 485 **Figure 10.** Trace-element patterns in Panasqueira tourmaline 1. **A.** Box plots of LA-ICP-MS results for tourmaline 1a  
 486 and 1b. The full box represents the lower quartile to upper quartile interval. The whiskers represent the 5%-95%  
 487 interval. Black circle: average value, black vertical line: median value. Open circle: outlier value, comprised in the 5%  
 488 lowest or highest data. Inset: normalization of average values of Tur1a to the Tur1b reference. **B.** Comparison of trace-  
 489 element distribution (average values) between Panasqueira tourmaline 1a and Beira schists. The elements are arranged  
 490 from left to right in accordance with their increasing concentration in tourmaline 1a. Data for Beira schists are from De  
 491 Amorin (2017), Bussink (1984), Oosterom et al. (1984), Pinto (2014) and Valladares et al. (2002).

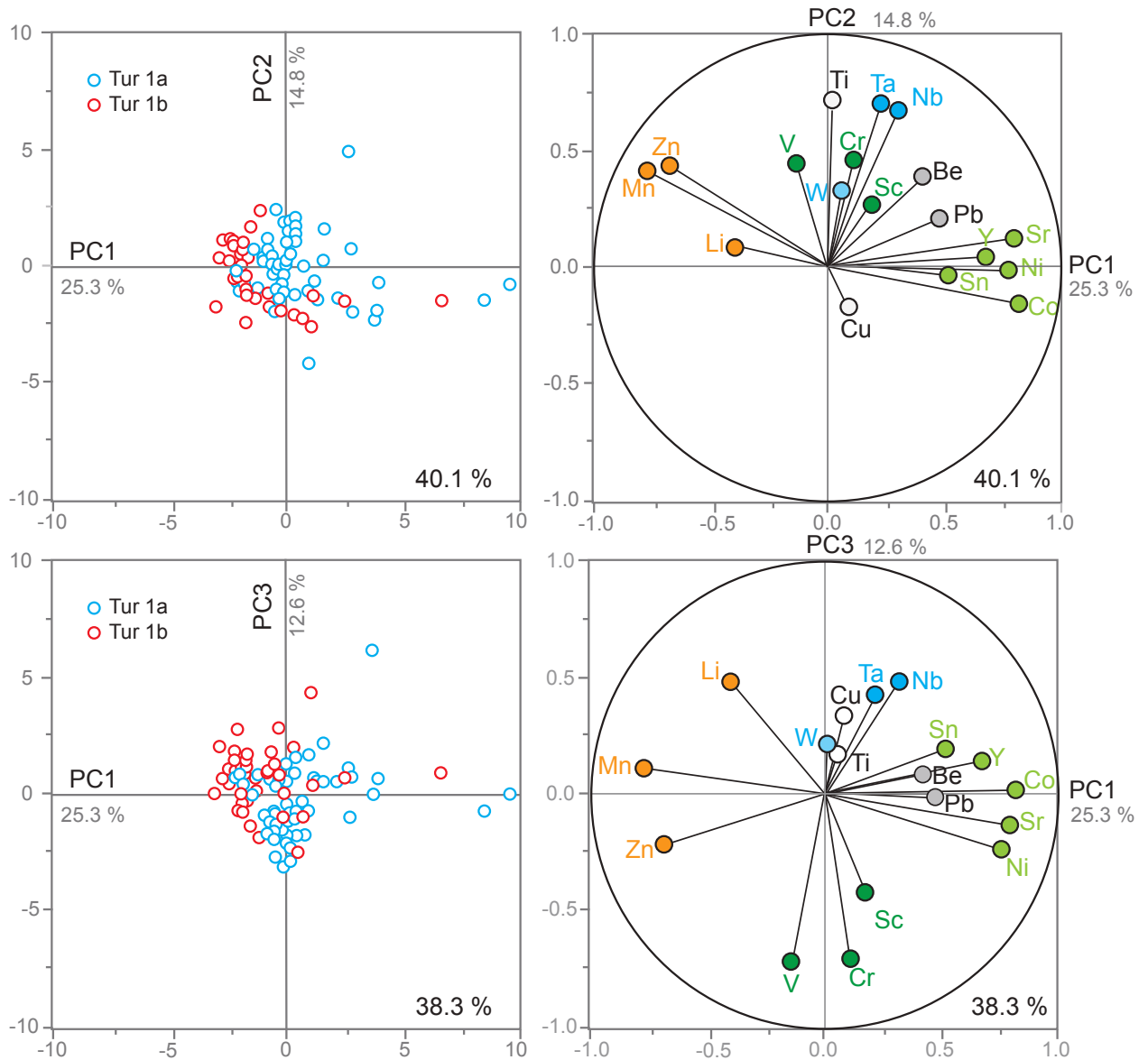
492  
 493 From Figure 10-A, it can be seen that Tur1a and Tur1b compositions are quite similar, although  
 494 there are minor but significant differences between them with most of the trace elements being



495  
 496 **Figure 11.** Chondrite-normalized REE profile for the Panasqueira tourmaline (samples PAN-I-3-c2 and PAN-III-8-  
 497 c1) compared to the profiles for the Panasqueira metasediments (1: De Amorin, 2017), the fluids associated to the  
 498 Sarekoubu orogenic gold deposit (2: Xu et al., 2008), the Yellowstone spring water (3: Lewis et al., 1997) and  
 499 magmatic-derived fluids (4: Banks et al., 1994; 5: Poitrasson et al., 1995) (explanations in the text).

500  
 501 depleted in Tur1b relative to Tur1a. The notable exceptions to this are Li, Mn and Zn, which are  
 502 depleted in Tur 1a. This is also evident from the differences in the average values (Table 1, and  
 503 insert in Figure 10-A), and from the shift between the full boxes (lower quartile to upper quartile  
 504 interval) in the box plot of Figure 10-A.

505 A principal component analysis was performed on the trace element data (using the JM Pro  
 506 software), the results of which are presented in Figure 12. Three axes (PC1-3) explain 52.7 % of the



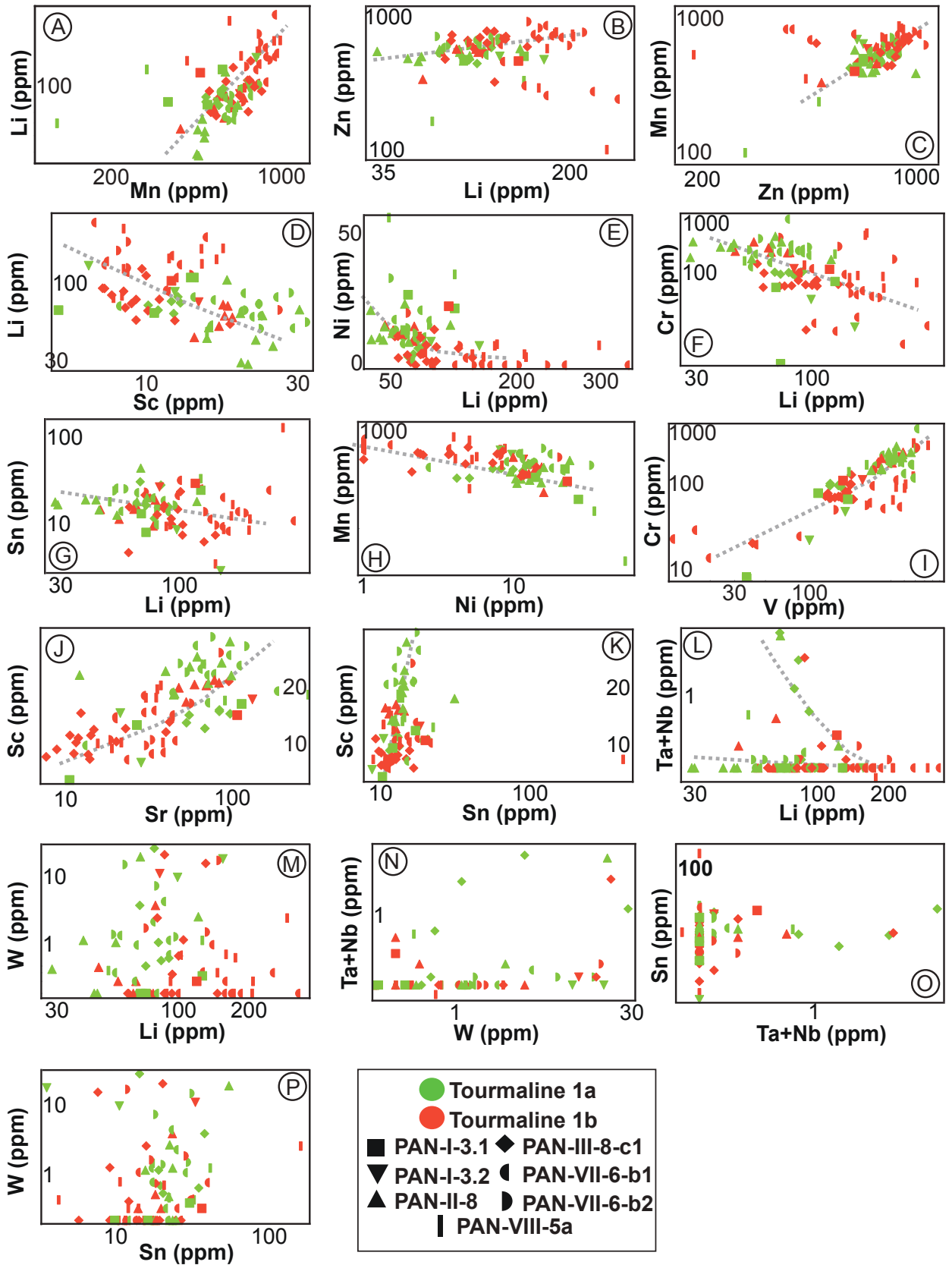
507

508 **Figure 12.** PCA analysis of the trace element composition of the Panasqueira tourmaline, allowing the definition of  
 509 several groups of trace elements, namely: Mn-Zn-Li, Cr-V-Sc, Co-Ni-Sr-Y-Sn, Be-Pb, and Nb-Ta (explanations in the  
 510 text).

511

512 variance. The first axis (PC1) clearly distinguishes Tur 1a and 1b, as well as two groups of  
 513 elements: a group A (Li-Mn-Zn) and a group B (nearly all other elements) reproduce, as expected,  
 514 the relationship observed in Figure 10. The PC2 and PC3 axes display correlations within group B,  
 515 providing evidence of several subgroups, namely: Co-Ni-Sr-Y-Sn, Cr-V-Sc, Nb-Ta and Pb-Be.  
 516 Copper, Ti, and W behave independently, and W appears uncorrelated to Nb-Ta.

517 In binary plots, elements of group A display rough linear trends expressing positive correlations  
 518 (when outliers are excluded), as seen for example in Figures 13-A to C, and predicted by the  
 519 principal component analysis. Similarly, elements of group A display negative correlations with  
 520 elements of group B, as seen, for example, in Figures 13-D to H. Less expected were the linear



521

522 **Figure 13.** Binary plots of selected trace elements from Panasqueira tourmaline, showing contrasting behaviour,  
 523 including positive, negative and null correlations, depending on the elements (explanation in the text).

524

525 relationships between elements from the various B subgroups, as seen for example in Figures 13-I  
526 to K. The rare metals (W, Nb, Ta) behave differently. Whereas Nb-Ta show a very loose negative  
527 correlation with Li (Fig.13-L), there is no correlation between W and Li (Fig. 13-M), nor between  
528 W and Nb-Ta (Fig. 13-N). Finally, Sn is not correlated with Nb-Ta (Fig. 13-O) or with W (Fig. 13-  
529 P).

530

### 531 ***Rutile composition:***

532 The composition and zoning of the Panasqueira rutile have been described in detail in Carocci et  
533 al. (2019) and only a summary is given here. This rutile contains variable proportions of: Fe from  
534 0.18 to 2.95 wt%, V from <1000 ppm to 3.48 wt%, Cr from <1000 ppm to 2.41 wt%, Nb from  
535 <1000 ppm to 1.64 wt%, Ta from <1000 ppm to 2.17 wt%, and W from 0.20 to 10.7 wt%. Despite  
536 locally high values, Nb and Ta concentrations are usually low; the Nb+Ta content is usually < 0.5  
537 wt% and the Nb/Nb+Ta ratio varies from 0.05 to 0.97 (on average 0.6).

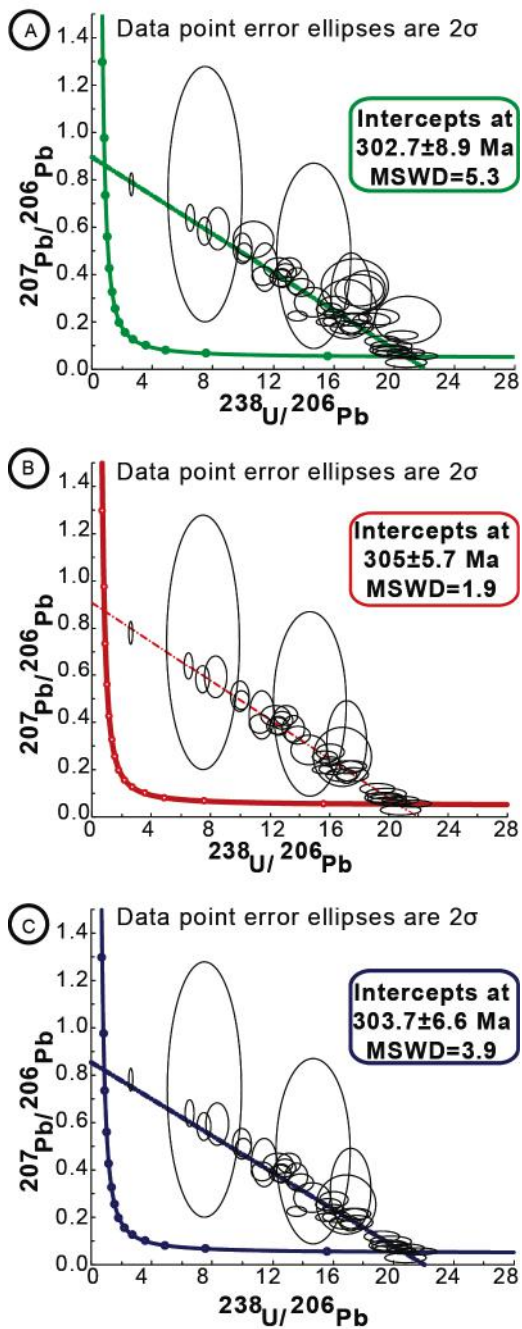
538 The crystals display marked sector zoning, exhibited mostly by W and Fe and, to a lesser extent,  
539 by Nb and Ta; Sn, V (and Cr), and display less evidence of zoning (Fig. 6- C to G). The maximum  
540 W concentration varies from 1.12 to 10.7 wt.% in the metal-rich sectors, depending on the sample;  
541 W concentrations in the metal-poor sectors vary between 0.26 to 1.40 wt %. As metal-rich sectors  
542 reach their highest W contents in wall rocks adjacent to veins in which wolframite is abundant,  
543 whereas in barren wall rocks the metal-rich sectors are less endowed in W (no more than 3.5 wt%  
544 W), it would appear that the W enrichment in rutile is related to the wolframite endowment in the  
545 nearby veins. Association of a very W-rich rutile with wolframite was also observed in the Puy-les-  
546 Vignes breccia-pipe tungsten deposit in the French Massif Central (Harlaux, 2016).

547 The sector zoning is superimposed on a conspicuous compositional zoning, expressed from the  
548 crystal scale down to the 10  $\mu\text{m}$  to  $\mu\text{m}$  scale of the doublets characteristic of oscillatory zoning (Fig.  
549 6-C). The zoning, however, is qualitatively and quantitatively the same irrespective of the rutile  
550 setting. All the minor elements, W, Nb(Ta), Fe, V, Cr and Sn, are involved in the compositional  
551 zoning. At all scales, W and Nb(Ta) are inversely-correlated, whereas Sn and V display inconsistent  
552 behavior, being either correlated with Nb(Ta) and inversely-correlated with W or the opposite.

553 The bulk evolution during crystal growth was variable from one crystal to the next, even at the  
554 sample scale. In some crystals, there is continuous evolution from a Nb-rich and W-poor core to a  
555 Nb-poor and W-rich rim, whereas the opposite is observed in others. Most commonly, however, the  
556 zoning displays moderate deviations from the average W content.

557

### 558 ***Age determinations***



559

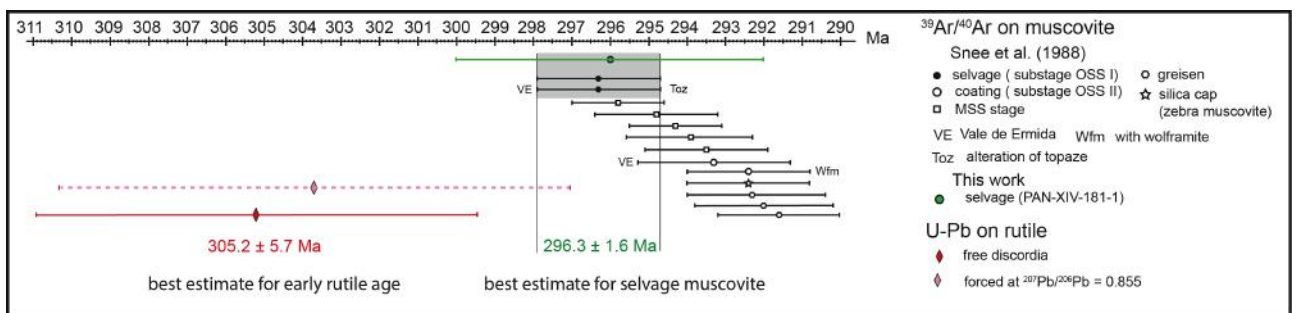
560 **Figure 14.** Results of U-Pb age determinations of wall-rock Panasqueira rutile (Tera-Wasserburg Concordia  
 561 diagrams). Note the highly discordant behaviour of the rutile. **A.** All data, showing the importance of lead loss in the  
 562 rutile crystals. **B.** Data remaining after elimination of analyses more affected by lead loss. **C.** Idem, with data  
 563 constrained to be consistent with the common lead value of Stacey and Kramers (1975) at c. 300 Ma. Explanations in  
 564 the text.

565

566 *Rutile:* Petrographic examination suggests that rutile from both the tourmalinized wall rocks and  
 567 the Qcs veinlets were coeval with the early tourmaline and the earliest wolframite deposition.  
 568 Unfortunately, the number of rutile crystals suitable for U-Pb dating was limited by the size of the  
 569 laser spot (45  $\mu\text{m}$ ). Some crystals from Qcs crack-seal veins are large enough to be analyzed, but

570 very few crystals in the wall rocks reach 50  $\mu\text{m}$  in diameter. Thus, only 22 crystals from 5 samples  
571 could be analyzed for their U-Pb isotopic compositions.

572 The analyzed crystals have variable concentrations of common lead, and low radiogenic Pb  
573 contents (Appendix 6, Table A6). On a Tera-Wasserburg diagram they plot in a discordant to a very  
574 discordant position, except for one sample (PAN-III-8-c1), which plots close to the Concordia  
575 curve. Figure 14 illustrates three regression lines: (i) using all the data, the regression line results in  
576 a discordia with a lower intercept at  $302.7 \pm 8.9$  Ma ( $2\sigma$ , MSWD = 5.3) (Fig. 14-A), the poor quality  
577 of this age determination being due to large lead losses, (ii) a discordia in which data corresponding  
578 to the greater lead losses were ignored (Fig. 14-B), passes through the concordant data and yields a  
579 lower intercept at  $305.2 \pm 5.7$  Ma ( $2\sigma$ , MSWD = 1.9), the upper intercept yielding a common lead  
580  $^{207}\text{Pb}/^{206}\text{Pb}$  ratio of 0.906, which is slightly higher than the 0.855 value predicted by the Stacey and  
581 Kramers (1975) model for the same age; and (iii) a discordia, anchored to the Stacey and Kramers  
582 composition at 305 Ma, yielding a lower intercept at  $303.7 \pm 6.6$  Ma ( $2\sigma$ , MSWD = 3.9) (Fig. 14-  
583 C). A similar date of  $303.7 \pm 6.6$  Ma, with a slightly higher MSWD value of 3.9 is obtained by  
584 constraining the regression to fit the Stacey and Kramers (1975) common lead composition,. A  
585 critical issue is the  $^{207}\text{Pb}/^{206}\text{Pb}$  value of the common lead in the CIZ at c 305 Ma. At c. 320 Ma, the  
586  $^{207}\text{Pb}/^{206}\text{Pb}$  ratio of the Ediacaran and Tremadocian metasediments was between 0.885 and 0.96  
587 (calculated from Nägler et al. 1993, 1995 data). It thus evident that the 0.906 value for the common  
588 lead in the Panasqueira rutile is in accordance with the regional values, and, consequently, the date  
589 of  $305.2 \pm 5.7$  Ma is interpreted as the best estimate for the crystallization age of the rutile. As  
590 Polya et al. (2000) demonstrated that the Qcs veins immediately preceded the main opening of the  
591 quartz vein system and wolframite deposition, the age of c. 305 Ma is also interpreted to be the age  
592 of the main wolframite deposition.



593  
594 **Figure 15.** Synthesis of radiometric ages for the Panasqueira deposit, comparing results of the present work with  
595 those of Snee et al. (1988). Explanation in the text.

596  
597 *Complementary dating:* To complement the U-Pb age determinations, a muscovite selvage  
598 (sample PAN-XIV-181-1) was dated using the  $^{39}\text{Ar}/^{40}\text{Ar}$  method at the University of Manitoba

599 (Canada) and yielded a good plateau age of  $296 \pm 2$  ( $1\sigma$ ) Ma, which is indiscernible within the limits  
600 of error (Appendix A7-Table A7) from the preceding  $^{39}\text{Ar}/^{40}\text{Ar}$  age of  $296.3 \pm 0.6$  Ma ( $1\sigma$ ) obtained  
601 by Snee et al. (1988) on muscovite selvages. Until now, this age was considered to be the age of the  
602 main mineralization (OSS stage of Polya et al., 2000), assuming that this muscovite preceded  
603 wolframite deposition. The new results show, however, that the muscovite selvages are at least 2  
604 Ma younger.

605

606

## Discussion

607

### *Tourmalinization: one or two fluids?*

#### *Tourmaline as a fluid proxy*

610 According to von Goerne et al. (2001), van Hinsberg (2011), Berryman et al. (2016) and  
611 Vereshchagin et al. (2018), the trace element partition coefficients between tourmaline and the  
612 medium from which it crystallizes are close to unity. Thus, the relative proportions of the trace  
613 elements in tourmaline reflect the relative proportions of trace elements in the fluid from which it  
614 crystallized. Fluorine concentration is subject to crystallographic constraints, because of its  
615 dependence on the X-charge in the structural formula (Henry and Dutrow, 2011). Within these  
616 constraints, the incorporation of F into the tourmaline structure is controlled by external factors, in  
617 particular, the F availability, and thus tourmaline may also be considered a F proxy.

618 In the absence of measurable fluid inclusions (FI) in the tourmalinized wall rocks at Panasqueira,  
619 information on the nature of the fluids responsible for the tourmalinization can be obtained  
620 indirectly, using the tourmaline composition. The major and trace element concentrations differ  
621 from Tur1a to Tur1b, pointing to a change in the fluid composition. Consideration of Figure 8-A  
622 and 10-A shows a shift from a Co, (Cu), Pb, Sc, Sr, V, Cr, Sn, Nb, Ta package in Tur1a, towards a  
623 Li, Fe, Mn, Zn, W rich package in Tur1b. The correlations shown in Figure 13 are clear evidence of  
624 a continuous evolution. This evolution could, however, have resulted from either the differentiation  
625 of a single fluid or the mixing between two fluid end-members.

#### *Discussion of single fluid models*

627 Single fluid models for the Panasqueira system have been favored by previous workers (Bussink,  
628 1984; Lecumberri-Sanchez et al., 2017; Codeço et al., 2017). Codeço et al. (2017) assumed that the  
629 Fe# increase was the result of a decrease in the temperature of a single fluid, from  $\sim 480^\circ\text{-}460^\circ\text{C}$   
630 during alteration of the wall rocks to  $360^\circ\text{-}230^\circ\text{C}$  in the mineralized quartz veins. The former  
631 temperature was estimated using the Ti-in-quartz thermometer (Codeço et al., 2017), whereas the  
632 latter come from earlier fluid inclusion studies (e.g., Kelly and Rye, 1979). Recent fluid inclusion

633 studies (Dejean, 2017; Cathelineau et al., 2017; 2018; Carocci, 2019) have concluded, however, that  
634 the temperature of the main quartz-wolframite deposition stage was  $450^{\circ}\pm 50^{\circ}\text{C}$ . Therefore, a strong  
635 temperature decrease cannot be the explanation for the change in Fe#.

636 Lecumberri-Sanchez et al. (2017) related the wolframite deposition to wall rock alteration. They  
637 concluded that the muscovitized parts, which commonly (but not systematically) fringe the  
638 mineralized quartz veins were coeval with the more distal tourmalinized zone, and that wolframite  
639 deposited due to the interaction of a Fe-poor, but W-bearing fluid, with the schists as a result of the  
640 release of Fe from the latter during muscovitization. This model is unsupported because: (1)  
641 muscovitization at the vein borders post-dated tourmalinization (see above), (2) the muscovitized  
642 fringes formed synchronously with the muscovite selvages of the mineralized quartz veins, and (3)  
643 the geochronological data reported in this study show that muscovite formed later than the wall-  
644 rock tourmalinization.

645 A fractional crystallization model could explain the Fe# increase from Tur1a to Tur1b but would  
646 require that the system was closed, which is inconsistent with the crack-seal textures of the Qcs  
647 veinlets associated with fluid influx into the wall rocks. It is difficult to reconcile this model with  
648 the differential behavior of the trace elements between Tur1a and Tur1b, some having been  
649 enriched, and others impoverished, something which cannot be explained by the effect of  
650 differences between partition coefficients. This model also explains the significant overlap of the  
651 trace element compositions of Tur1a and Tur1b (Fig. 13).

652 A final single fluid model that could be considered is one in which the system evolved  
653 continuously from wall rock-controlled (Tur0) to fluid-controlled (Tur1b stage) conditions during  
654 the course of fluid-rock interaction. High water-rock ratios are indicated by the absence of  
655 compositional differences in either the Tur1a or Tur1b zones, with respect to the position of  
656 tourmaline in the system, irrespective of whether the tourmaline is in Qcs veinlets or part of the  
657 tourmalinized wall rock, proximal or distal to the veinlets. Furthermore, the widespread evidence of  
658 corrosion of the Tur0 cores points to sudden changes in the ambient fluid composition, which is  
659 difficult to reconcile with the single fluid model. During such fluid-rock interaction, the Tur0  
660 composition would reflect the host-rock composition prior to the alteration, masking the  
661 characteristics of the incoming fluid. Petrographic observations indicate that tourmaline grew at the  
662 expense of earlier ferro-magnesian minerals (biotite, cordierite). Thus, the Fe# in the Tur0 cores  
663 would be expected to reflect the Fe# of the Beira schist, which is not the case (Fig. 8A). In addition,  
664 the lack of F in Tur0 is in strong contrast with the high F content of the Beira schists (570 ppm in  
665 average: Oosterom et al., 1984). Also, despite the high Ti content (0.6 to 1.0 wt%  $\text{TiO}_2$ ) of the Beira  
666 schists (Bussink, 1984), the tourmaline is Ti-poor, which may, however, be due, at least in part, to

667 competition with the coeval rutile. The Tur1a and Tur1b trace element package is, in order of  
668 decreasing abundance (Figure 10-A): Ti-Zn-Mn-(V, Cr)-(Sr,Li)-Sn-(Sc,Ni)-Be-Pb-W-(Cu,Co)-Y-  
669 Nb-Ta. A compilation of local data (Figure 10-B) reveals that in the Beira schists, these elements  
670 are in a significantly distinct order of decreasing abundance: Ti-Mn-(Zn,V,Li)-(Cr,Sr)-Ni-Cu-  
671 (Co,Y,Sc)-Nb-Pb-(W,Sn)-Be-Ta. Therefore, concentrations in Tur0 and Tur1a are not strictly  
672 mimetic of the Beira schist composition.

673 In conclusion, no single fluid evolution model is able to fully explain all the data, and a two-fluid  
674 model must be seriously considered.

#### 675 *A two-fluid mixing model*

676 We propose a fluid-mixing model involving two end-members, the first of which (F1) was  
677 associated with the formation of Tur0, and the second (F2) of which mixed with F1 to form Tur1a  
678 and then Tur1b. The F1 fluid end-member composition, like Tur1a, was enriched in Co, (Cu), Pb,  
679 Sc, Sr, V, Cr, Sn, Nb, Ta, depleted in F and more magnesian than F2. The F2 fluid end-member  
680 composition, like Tur1b, was enriched in Li, Mn, Zn, Fe and F (Fig. 7-D). As tungsten  
681 concentration does not correlate with that of Nb, Ta and Sn (Fig. 12 and 13), we propose that it was  
682 enriched in the F2 fluid, despite the fact that Tur1b is generally depleted in W relative to Tur1a  
683 (Fig. 10-A) and attribute this apparent contradiction to competition for tungsten between Tur1b and  
684 the coeval W-rich rutile. This proposal is supported by the abundance of W-bearing nano-inclusions  
685 in Tur1b (as inferred from tungsten anomalies in the LA-ICP-MS record, see above) and the  
686 occurrence of the coeval W-rich rutile.

687 The fluid-mixing model explains the inter-element correlations and anti-correlations displayed in  
688 Figure 13. The corrosion exhibited by the Tur0 core may mark the arrival of F2 into the system and  
689 the onset of the mixing process. The evidence for a continuous process and the conflicting evidence  
690 of a sharp transition between Tur1a and Tur1b, could indicate a sudden increase in the F2 to F1  
691 fluid ratio. This increase could have been related to an interruption in deposition due to a temporary  
692 closure of the vein system. Local corrosion, or overprinting (Fig. 9), of Tur1a by Tur1b is a further  
693 evidence for this explanation. The small scale oscillations of Fe# during crystal growth, as well as  
694 the recurrence of low Fe# at the end of the Tur1b growth, could reflect also temporary variations in  
695 the F2 to F1 fluid ratio, explaining the overlap between Tur1a and Tur1b trace element  
696 compositions in Figure 13.

697

#### 698 *The fluid source*

699 *Magmatic or metamorphic source: boron and REE constraints*

700 *Boron:* the boron in tungsten deposits is usually considered to be of magmatic origin (e.g.,  
701 London, 2011), and this interpretation has been adopted for Panasqueira in the recent works of  
702 Lecumberri-Sanchez et al. (2017), Codeço et al. (2018) and Launay et al. (2018). According to  
703 these studies, fluids released from the Panasqueira granite, and in particular, from the greisenized  
704 cupola, provided the boron required for tourmalinization. Codeço et al. (2017) reported that the  
705  $\delta^{11}\text{B}$  values of the Panasqueira tourmaline are between -4‰ and -13‰ (with 90% of the data  
706 between -7‰ and -11‰) and display a Gaussian distribution. These values are consistent with  
707 either a magmatic or a metasedimentary source for the boron.

708 Tourmaline replaced the contact metamorphic aureole minerals related to the emplacement of the  
709 main Panasqueira granite, and is therefore later than this magmatic stage. Consequently,  
710 tourmalinization is unlikely have been caused by magmatic fluids issued from this large body by  
711 itself. In fact, the cupola, as well as the sheet-like body of rare metal granite (RMG) type, at the top  
712 of the main granite body (De Amorin, 2017), may have been emplaced later, and, consequently may  
713 have been a source of boron, and the fluid to transport it. A mass balance calculation (details  
714 presented in Appendix A8) shows that the cupola could not by itself have supplied the quantity of  
715 boron needed for wall rock tourmalinization, at the deposit scale. By the same calculation, the  
716 subjacent sheet-like RMG body could, however, have supplied a significant part of this boron,  
717 although certainly not all that was required. The calculations were done under the assumption of a  
718 tourmaline-saturated melt. Yet, tourmaline is typically absent from the cupola or the subjacent  
719 RMG, and observation of the cupola/schist contact did not reveal evidence for tourmalinization of  
720 the wall rock. The calculated B deliveries are therefore greatly overestimated. Another problem is  
721 the volume of fluid that was needed for tourmalinization. The Panasqueira RMG sheet-like body  
722 could only have supplied an order of magnitude less than the required volume of fluids (Appendix  
723 A8). Another source of boron (and fluids) is clearly required.

724 Concentrations of boron are around 0.5 to 1%, at tourmaline saturation in aqueous fluids  
725 buffered in respect to aluminium silicate at temperatures between 500 and 600°C, according to  
726 experimental data (Weisbrod et al., 1986; London, 2011). Consequently, metamorphic fluids may  
727 have the capacity to extract and transport boron. The Beira schists contain on average ~ 100 ppm B  
728 (Oosterom et al., 1984). Mass balance calculations (Appendix A8) show that the 410 to 810 kt of  
729 boron required to account for the observed tourmaline, and the 2.2 to 4.3 km<sup>3</sup> of fluid, necessary to  
730 dissolve, transport and deposit this amount of boron, may be produced by the devolatilization of no  
731 more than 20 km<sup>3</sup> to 40 km<sup>3</sup> of Beira schists.

732 *Rare earth elements:* the REE profiles of Tur1 are very similar to those of the Beira schists (Fig.  
733 11), suggesting that the fluids responsible for tourmalinization were of metamorphic origin or

734 equilibrated with metasedimentary rocks at high temperature. Similar REE profiles are observed in  
735 tourmaline from deposits for which a metamorphic origin of the fluid is accepted, as for example  
736 the orogenic gold deposit of Sarekoubu (Xu et al., 2008) (Fig. 9). In contrast, magmatic-  
737 hydrothermal fluids, as well as fluids that equilibrated with granite at a high subsolidus temperature,  
738 display a pronounced negative europium anomaly (e.g., Banks et al., 1994; Poitrasson et al., 1995),  
739 which is absent from the REE patterns of Panasqueira tourmaline (Fig. 11). A significant magmatic  
740 contribution to the tourmalinizing fluids is therefore unlikely.

741

#### 742 *Distinguishing F1-F2 fluids: trace elements constraints*

743 The characteristic Ti, V, Cr, Sr, Sn, Sc, Pb, Ni, Be, Co, Cu, Y, Nb, Ta trace element package  
744 deduced for the F1 end-member in a preceding section is consistent with F1 having been  
745 equilibrated with a metasedimentary sequence like the Beira Schists. Indeed, it is known that  
746 metamorphic fluid compositions reflect those of the related metamorphic rocks (e.g., Tang and Liu,  
747 2002).

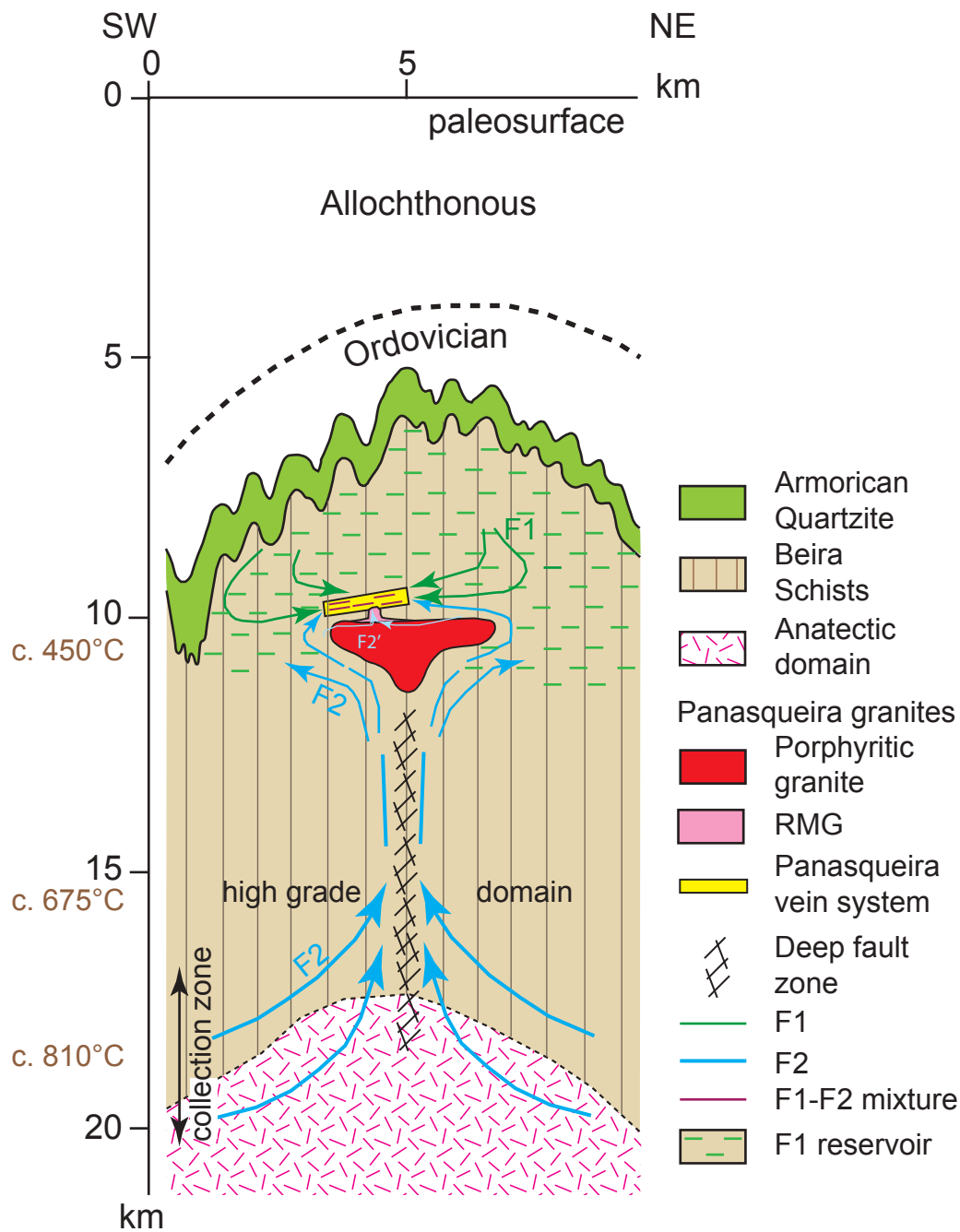
748 The F2 composition characterized by the Fe, F, Mn, Li, Zn, W package could suggest  
749 equilibrium with a granitic magma. Magmatic fluids issued from RMG melts (e.g., Harlaux et al.,  
750 2017) rich in F, Li, Fe and Mn, however, are richer in Sn than W, contain similar W and Nb-Ta  
751 contents, and are depleted in Zn. These significant differences with the F2 package consequently do  
752 not support a magmatic origin for the F2 fluid.

753 This apparent paradox may be resolved in the context of the processes occurring in the CIZ  
754 middle crust at the end of the Carboniferous. Dehydration-melting in migmatite domains involving  
755 biotite breakdown and the formation of granitic melts (Pereira Gomez et al., 2000) likely took place  
756 at the end of the Carboniferous, as in equivalent domains of the Variscan belt at this time (e.g.,  
757 Gutierrez-Alonso et al., 2011; Barbey et al., 2015). It is known that biotite from the high-grade  
758 (unmelted) Beira schists contains significant proportions of F, Li, as well as Fe, Mn, Zn and W  
759 (Acosta-Vigil et al., 2011). Biotite breakdown is therefore a potential source for Li, F, Fe, Mn, Zn,  
760 and rare metals. The dehydration-melting anatectic domains are also potential sources of large fluid  
761 volumes (larger than those released by most granite plutons), produced only through the biotite  
762 incongruent melting. During crystallization of the haplogranitic leucosome melt, the unmixed  
763 migmatitic fluid would therefore bear the biotite signature in trace elements. This signature, which  
764 differs from that of metamorphic fluids issued from unmelted areas, is consistent with the F2 trace  
765 element package. Final melting of tourmaline in the anatectic domains delivered boron (Acosta-  
766 Vigil et al., 2011), and thus F2 may have contained the boron required for the Tur1b crystallization.

767

768 ***Proposed conceptual model***

769 In order to integrate the preceding results into a workable model for the tourmalinization at  
770 Panasqueira, a starting point is to consider the upward transfer of the boron-rich F2 fluid from the  
771 inferred source at depth to the deposit level. Here, the concept of a mid-crustal channelized fluid  
772 flow (Connolly, 1989) may be called for. According to the modelling by Connolly (1989), deep  
773 fluids issued from biotite dehydration gather into a collection zone, and are then focused and  
774 channelled into a mid-crustal fault zone, ascending at high rates up to a dispersion region in cooler  
775 rocks. The half-width of the collection and dispersion zones is typically in the 3-5 km range, and the  
776 height of the system is on the order of 10 to 15 km. The flow results in upward heat advection on a  
777  $\sim 10^4$  yr time-scale, inducing a temperature increase of several 10s °C at the 100 kyr time-scale in  
778 the dispersion region (Connolly, 1989).



779

780 **Figure 16.** Conceptual model of the crustal scale hydrothermal system at the onset of the main wolframite stage at  
 781 Panasqueira. A geothermal gradient of  $\sim 40^{\circ}\text{C.km}^{-1}$  is assumed (Cathelineau et al., 2018). The model involves two  
 782 sources of metamorphic fluids at different structural levels (F1 and F2), and their mixing in the Panasqueira vein  
 783 system. Explanations in the text.

784

785 Applied to the Panasqueira system, the collection domain of this model could have been located  
 786 at depths of 15-20 km, where F2 fluids could have been generated by incongruent melting of  
 787 biotite. With a total width of 10 km, such a collection domain would have been large enough to  
 788 provide both the required mass of boron and the fluid volume for tourmalinization. The fault zone  
 789 necessary for the channelling is thought to have been related to the emplacement of the main

790 Panasqueira granite. Owing to the NNW-SSE elongation of the body (Ribeiro, 2017), this  
791 postulated fault should have a similar direction. In addition, fluid ascent was facilitated by the  
792 vertical permeability ( $S_0$  and schistosity) in the core of the Panasqueira anticline.

793 At a level corresponding roughly to the bottom of the dispersion level of Connolly (1989), the  
794 ascending F2 fluid encountered the Panasqueira granite body and was forced around it, as a  
795 consequence of the thermal boundary layer hindering penetration of the flowing fluids into the  
796 granite body (this implies that the initiation of the hydrothermal system immediately succeeded  
797 granite emplacement). Thereafter, it was driven towards the main permeability channel (the system  
798 of joints that guided the future vein system), where it met the resident fluid. As seen in Figure 16, at  
799 c. 305 Ma, a continuous cap of thick impermeable Ordovician quartzite (Armorican Quartzite)  
800 covered the Beira schists, defining a reservoir for the metamorphic fluids released by either the first  
801 LP-HT event in the CIZ at c. 320-317 Ma or by the contact metamorphism of the main Panasqueira  
802 granite or both. These fluids are interpreted to represent the F1 end-member. The continuous  
803 transfer of heat by the F2 fluid and the resulting heating of the dispersion zone (Connolly, 1989), is  
804 thought to have driven convective flow of F1 in the Panasqueira reservoir, promoting the mixing of  
805 F1 with F2 fluids in the high permeability domain, which resulted in tourmaline deposition (Fig.  
806 16). Cooling of the Panasqueira granite pluton, could have contributed to the thermal anomaly.  
807 Launay et al. (2018) described an outwardly flow pattern in the close vicinity of the “greisen  
808 cupola”, which they interpreted as the radial flow of magmatic fluids out from the cupola. As  
809 suggested in Figure 16, this remarkable pattern could as well have resulted from the limited  
810 penetration of the F2 fluid in the uppermost granite layers (F2' pattern in Figure 16). Because the  
811 F2 input may have varied with time, the model in Figure 16 is consistent with the short-term  
812 variations in the F1 to F2 ratios that are inferred from the rutile zoning and tourmaline profiling.

813

814

## Conclusions

815

816 1. The earliest hydrothermal event in the Panasqueira system was wall rock tourmalinization.  
817 Zoned tourmaline replaced ferro-magnesian minerals in the protolith in a Tur0-Tur1a,b sequence.  
818 This event coincided with the first fluid-overpressure-induced opening of crack-seal fractures (Qcs  
819 veinlets).

820 2. The early Tur1 tourmaline, and in particular, the development of Tur1b rims, was coeval with  
821 the formation of W-bearing rutile (which is among the richest in W anywhere) and the first  
822 appearance of wolframite.

823 3. On the basis of a limited number of observations, it seems that there is a correlation between  
824 the presence/abundance of wolframite in quartz veins and the relative importance in the adjacent  
825 altered wall rock of Tur1b rims, and a high content of tungsten in rutile. The poor development of  
826 the Tur1b rim, and limited W enrichment in the rutile, together with the presence of ilmenite  
827 lamellae, are indicators of barren veins. This is of potential interest for evaluating exploration drill  
828 holes from a resource and mine development perspective.

829 4. The early rutile crystallized at  $305.2 \pm 5.7$  Ma and coincided with early tourmalinization and  
830 the first appearance of wolframite. This new age is greater than the currently accepted age of c. 296  
831 Ma, which was obtained on muscovite selvages that post-dated wolframite deposition.

832 5. The Panasqueira hydrothermal system was active for more than 6-8 Ma and was the product  
833 of a much deeper crustal system than proposed in previous studies, in which the W mineralizing  
834 fluids were released by a single granite intrusion.

835 6. Two fluids, both of metamorphic origin, were involved in tourmaline growth. The first, rich in  
836 Ti, V, Cr, Sr, Sn, Sc, Pb, Ni, Co, Cu, Y, Nb, Ta, and of “local” derivation, was replaced  
837 progressively by a second fluid, rich in Li, F, Fe, Mn, W, of deeper origin (biotite dehydration).  
838 This second fluid carried the metals necessary for wolframite deposition and in particular Fe and  
839 Mn, which were not inherited from the host rocks.

840

841

### Acknowledgements

842 EG Berryman and in particular AE William-Jones are thanked for constructive criticism and  
843 detailed suggestions that helped to improve the first drafts of the manuscript. Additional corrections  
844 from F. B. Wadsworth (Durham University) and A. Samper (OTELO, Lorraine University) were  
845 greatly appreciated.

846 This work benefited from the analytical capabilities of the GeoRessources Laboratory  
847 (Université de Lorraine, CNRS, CREGU), and the authors gratefully acknowledge Olivier Rouer,  
848 Andrei Lecomte, Lise Salsi and Chantal Peiffert for their technical help. LA-ICP-MS equipment  
849 was financed by CPER program (National Funds – Lorraine region – FEDER).

850 This work was financed by the ERAMIN project NewOres financed by ANR (ANR-14-EMIN-  
851 0001), and Labex Ressources 21 (supported by the French National Research Agency through the  
852 national program “Investissements d'avenir”) with reference ANR – 10 – LABX 21 —LABEX  
853 RESSOURCES 21.

854 We are most grateful to Beralt Tin and Wolfram S.A. for permitting access to the Panasqueira  
855 underground mine, and technical help during field work.

856

## References

- 857  
858
- 859 Acosta-Vigil, A., Pereira, M.D., Shaw, D.M., and London, D., 2011, Contrasting behaviour of  
860 boron during crustal anatexis: *Lithos*, v. 56, p. 15-31.
- 861 Alcock, J.E., Martínez Catalán, J.R., Rubio Pascual F.-J., Díez Montes, A., Díez Fernández, R.,  
862 Gómez Barreiro, J., Arenas, R., Dias da Silva, I., and Clavijo, E.G., 2015, 2-D thermal  
863 modeling of HT–LP metamorphism in NW and Central Iberia: Implications for Variscan  
864 magmatism, rheology of the lithosphere and orogenic evolution: *Tectonophysics*, v. 657, p.  
865 21-37.
- 866 Almonty Industries, 2016, Report NI 43-101. Technical report on the mineral resources and  
867 reserves of the Panasqueira mine, Portugal: [http://www.almonty.com](http://www.almonty.com/_resources/Panasqueira_43-101_Tech_Rep_Dec16_SEDAR.PDF)  
868 [/\\_resources/Panasqueira\\_43-101\\_Tech\\_Rep\\_Dec16\\_SEDAR.PDF](http://www.almonty.com/_resources/Panasqueira_43-101_Tech_Rep_Dec16_SEDAR.PDF).
- 869 Banks, D.A., Yardley, B.W.D., Campbell, A.R., and Jarvis, K.E., 1994, REE composition of an  
870 aqueous magmatic fluid: A fluid inclusion study from the Capitan Pluton, New Mexico,  
871 U.S.A: *Chemical Geology*, v. 113, p. 259-272.
- 872 Barbey, P., Villaros, A., Marignac, C., and Montel, J.M., 2015, Multiphase melting, magma  
873 emplacement and P-T-time path in late-collisional context: the Velay example (Massif  
874 Central, France): *Bulletin de la Société Géologique de France*, v. 186, p. 93–116.
- 875 Berryman, E.J., Kutzschbach, M., Trumbull, R.B., Meixner, A., van Hinsberg, V., Kasemann, S.A.,  
876 and Frantz, G., 2017, Tourmaline as a petrogenetic indicator in the Pfitsch Formation,  
877 Western Tauern Window, Eastern Alps: *Lithos*, v. 284-285, p. 138-155.
- 878 Bloot, C., and De Wolf, L.C.M., 1953, Geological features of the Panasqueira tin-tungsten ore-  
879 occurrence (Portugal): *Boletim da Sociedade Geologica de Portugal*, v. XI, p. 1-57.
- 880 Bosi, F., 2011, Stereochemical constraints in tourmaline: from a short-range to a long-range  
881 structure: *The Canadian Mineralogist*, v. 49, p. 17-27.
- 882 Bosi, F., 2018, Tourmaline crystal chemistry: *American Mineralogist*, v.103, p. 298-306.
- 883 Burnard, P.G., and Polyá, D.A., 2004, Importance of mantle derived fluids during granite associated  
884 hydrothermal circulation: He and Ar isotopes of ore minerals from Panasqueira: *Geochimica*  
885 *et Cosmochimica Acta*, v. 68, p. 1607–1615. doi:10.1016/j.gca.2003.10.008.
- 886 Bussink, R.W., 1984, Geochemistry of the Panasqueira tungsten-tin deposit, Portugal: *Geologia*  
887 *Ultraiectina*, v. 33, p. 1-159.
- 888 Carocci, E., 2019, Tungsten transport and deposition in magmatic-hydrothermal environments : the  
889 example of Panasqueira (Portugal): PhD Thesis, Univ. de Lorraine, 271 p.

890 Carocci E., Marignac C., Cathelineau M., Truche L., Lecomte A., and Pinto F., 2019, Rutile from  
891 Panasqueira (Central Portugal): an excellent pathfinder for wolframite deposition: *Minerals*,  
892 v. 9, 9; <https://doi.org/10.3390/min9010009>.

893 Castro, A., Corretge, L.G., de la Rosa, J.D., Fernández, C., López, S., García-Moreno, O., and  
894 Chacón, H., 2003, The appinite–migmatite complex of Sanabria, NW Iberian Massif, Spain:  
895 *Journal of Petrology*, v. 44, p. 1309–1344.

896 Cathelineau, M., Marignac, C., Rolland, J.-M., Boiron, M.-C., and Dejean, M., 2017, Are we sure to  
897 know the fluids responsible for W mineralization at Panasqueira (Portugal): the case for loss  
898 of information due to intense quartz recrystallization and FI natural decrepitation: European  
899 Current Research on Fluid Inclusions (ECROFI) Biennial Meeting, 24<sup>th</sup>, Nancy, France,  
900 Abstracts, p. 98.

901 Cathelineau, M., Marignac, C., Boiron, M.-C., Carocci, E., Rolland, J.-M., Dejean, M., Dourk, M.,  
902 and Pinto, F., 2018, Nouvelle approche du chemin P-T-t des fluides dans le gisement à W-Sn-  
903 Cu de Panasqueira (Portugal): persistence d'une anomalie thermique d'origine profonde en  
904 cours d'exhumation: Earth Science Meeting (RST), 26<sup>th</sup>, Lille, France, 2018, Abstracts, p.  
905 694.

906 Chew, D.M., Petrus, J.A., and Kamber, B.S., 2014, U-Pb LA-ICPMS dating using accessory  
907 mineral standards with variable common Pb: *Chemical Geology*, v. 363, p. 185-199.

908 Clark, A.H., 1970, Potassium-argon ages and regional relationships of the Panasqueira tin-tungsten  
909 mineralization, Portugal: *Servicos Geologicos Comunicacoes*, v. 54, p. 243-261.

910 Codeço, M.S., Weis, P., Trumbull, R.B., Pinto, F., Lecumberri-Sanchez, P., and Wilke, F.D., 2017,  
911 Chemical and boron isotopic composition of hydrothermal tourmaline from the Panasqueira  
912 W-Sn-Cu deposit, Portugal: *Chemical Geology*, v. 468, p. 1-16.

913 Connolly, J.A.D., 1989, Mid-crustal focused fluid movement: thermal consequences and silica  
914 transport, in Jamtveit, B., Yardley, B.W.D., eds, *Fluid flow and transport in rocks,*  
915 *mechanisms and effects: Chapman & Hall, London*, p. 235-250.

916 De Amarin, A., 2017, *Pétrographie géochimie des granitoides de la mine de W de Panasqueira*  
917 *(Portugal): Rôle dans la genèse des minéralisations: Unpublished M.Sc. thesis, Université de*  
918 *Lorraine (France), Laboratoire Géoresources, 37 p.*

919 Dejean, M., 2017, *Fluides minéralisateurs dans le gisement de Panasqueira: Reconstruction P-T-X:*  
920 *Master2 Univ de Lorraine, 31 p.*

921 Dias, G., Leterrier, J., Mendes, A., Simões, P.P., and Bertrand J.M., 1998, U-Pb zircon and  
922 monazite geochronology of post-collisional Hercynian granitoids from the Central Iberian  
923 Zone (Northern Portugal): *Lithos*, v. 45, p. 349-369.

- 924 Díez Fernández, R., and Pereira, M.F., 2017, Strike-slip shear zones of the Iberian Massif: Are they  
925 coeval?: *Lithosphere*, v. 9, p. 726-744.
- 926 Díez Fernández, R., Martínez Catalán, J.R., Barreiro, J.G., and Arenas, R., 2012, Extensional Flow  
927 during Gravitational Collapse: A Tool for Setting Plate Convergence (Padrón Migmatitic  
928 Dome, Variscan Belt, NW Iberia): *The Journal of Geology*, v. 120, p. 83-103.
- 929 Díez Fernández, R., Barreiro, J.G., Martínez Catalán, J.R., and Ayarza, P., 2013, Crustal thickening  
930 and attenuation as revealed by regional fold interference patterns: Ciudad Rodrigo basement  
931 area (Salamanca, Spain): *Journal of Structural Geology*, v. 46, p.115-128.
- 932 Díez Fernández, R., Arenas, R., Pereira, M.F., Sánchez-Martínez, S., Albert, R., Martín Parra, L.M.,  
933 Rubio Pascual, F.J., and Matas, J., 2016, Tectonic evolution of Variscan Iberia: Gondwana–  
934 Laurussia collision revisited: *Earth-Science Reviews*, v. 162, p. 269-292.
- 935 Fernández-Suárez, J., G. Gutiérrez-Alonso, S. T. Johnston, T. E. Jeffries, D. Pastor-Galan, G. A.  
936 Jenner, and Murphy, J.B., 2011, Iberian late- Variscan granitoids: Some considerations on  
937 crustal sources and the significance of “mantle extraction ages”: *Lithos*, v. 123, p. 121–132,  
938 doi:10.1016/j.lithos.2010.09.010.
- 939 Foxford, K.A., Nicholson, R., and Polya, D.A., 1991, Textural evolution of W–Cu–Sn bearing  
940 hydrothermal quartz veins at Minas da Panasqueira, Portugal: *Mineralogical Magazine*, v. 55,  
941 p. 435–445.
- 942 Foxford, K.A., Nicholson, R., Polya, D.A., and Hebblethwaite, R.P.B., 2000, Extensional failure  
943 and hydraulic valving at Minas da Panasqueira, Portugal: evidence from vein spatial  
944 distributions, displacements and geometries: *Journal of Structural Geology*, v. 22, p. 1065–  
945 1086, [http://dx.doi.org/10.1016/S0191-8141\(00\)00029-8](http://dx.doi.org/10.1016/S0191-8141(00)00029-8).
- 946 Garcia, D., 2004, Travaux présentés pour l’obtention du diplôme Habilitation à Diriger les  
947 Recherches en Sciences de la Terre et de l’Univers, Espace: Génie des procédés, Université  
948 Jean Monnet; Ecole Nationale Supérieure des Mines de Saint-Etienne, 87 p.
- 949 Gutiérrez-Alonso, G., Fernández-Suárez, J., Jeffries, T.E., Johnston, S.T., Pastor-Galán, D.,  
950 Murphy, J.B., Franco, P., and Gonzalo, J.C., 2011, Diachronous post-orogenic magmatism  
951 within a developing orocline in Iberia, European Variscides: *Tectonics*, v 30,  
952 doi:10.1029/2010TC002845.
- 953 Harlaux, M, 2016, Les systèmes métallogéniques hydrothermaux à tungstène et métaux rares (Nb,  
954 Ta, Sn) dans le contexte orogénique fini-varisque : exemple du Massif Central Français)  
955 (Tungsten and rare-metal (Nb, Ta, Sn) hydrothermal metallogenic systems in the late-  
956 Variscan orogenic context: example of the French Massif Central): PhD thesis, Université de  
957 Lorraine (France), Laboratoire Géoresources, 451 p.

958 Harlaux, M., Mercadier, J., Bonzi, W.M.-E., Kremer, V., Marignac, C., and Cuney, M., 2017,  
959 Geochemical signature of magmatic-hydrothermal fluids exsolved from the Beauvoir rare-  
960 metal granite (Massif Centra, France): insights from LA-ICPMS analysis of primary fluid  
961 inclusions: *Geofluids*, v. 2017, Article ID 1925817, 25 p. <https://doi.org/10.1155/2017/1925817>.  
962

963 Hawthorne, F.C., and Dirlam, D.M., 2011, Tourmaline the indicator mineral: From atomic  
964 arrangement to Viking navigation: *Elements*, v. 7, p. 307-312.

965 Henry, D.J., and Dutrow, B.L., 2011, The incorporation of fluorine in tourmaline: internal  
966 crystallographic controls or external environmental influence?: *The Canadian Mineralogist*, v.  
967 49, p. 41-56.

968 Henry, D.J., and Guidotti, C.V., 1985, Tourmaline as a petrogenetic indicator mineral: an example  
969 from the staurolite-grade metapelites of NW Maine: *American Mineralogist*, v. 70, p. 1-15.

970 Henry, D.J., Novák, M., Hawthorne, F.C., Ertl, A., Dutrow, B.L., Uher, P., and Pezzotta, F., 2011,  
971 Nomenclature of the tourmaline supergroup minerals: *American Mineralogist*, v. 96, p. 895–  
972 913.

973 Inverno, C.M.C., Ferraz, P.J.V., and Moreira, E., 2009, Argemela, a high-tonnage Sn-Li deposit in  
974 Central Portugal: Geological Society of America Annual Meeting, Portland, 2009, Abstracts  
975 41, p. 680.

976 Jacques, D., Vieira, R., Muchez, P., and Sintubin, M., 2018, Transpressional folding and associated  
977 cross-fold jointing controlling the geometry of post-orogenic vein-type W-Sn mineralization:  
978 examples from Minas da Panasqueira, Portugal: *Mineralium Deposita*, v. 53, p. 171-194.

979 Jaques, L., and Pascal, C., 2017, Full paleostress tensor reconstruction using quartz veins of  
980 Panasqueira Mine, central Portugal; part I: Paleopressure determination: *Journal of Structural*  
981 *Geology*, v. 102, p. 58-74.

982 Julivert, M., Fontboté, J.M., Ribeiro, A., and Nabais-Conce, L.E., 1972, Mapa tectónico de la  
983 Península Ibérica y Baleares, 1:1.000.000: IGME, Memoria explicativa, p. 113.

984 Kelly, W.C., and Rye, R.O., 1979, Geologic, fluid inclusion, and stable isotope studies of the tin-  
985 tungsten deposits of Panasqueira, Portugal: *ECONOMIC GEOLOGY*, v. 74, p. 1721–1822.

986 Kuhn, T., 2018, Al-in-Hornblende barometry of Southern New England intrusions and comparison  
987 with metamorphic bathograds: Senior Thesis, Department of Geology and Geophysics, Yale  
988 University, 25 p.

989 Lach P, Mercadier J., Dubessy J., Boiron M.C., Cuney M., 2013, In-situ quantitative measurement  
990 of rare earth elements in uranium oxides by Laser Ablation-Inductively Coupled Plasma-Mass  
991 Spectrometry. *Geostandards and Geoanalytical Research*. 37, 277-296

- 992 Launay, G., Sizaret, S., Guillou-Frottier, L., Gloaguen, E., and Pinto, F., 2018. Deciphering fluid  
993 flow at the magmatic-hydrothermal transition: A case study from the world-class Panasqueira  
994 W–Sn–(Cu) ore deposit (Portugal): *Earth and Planetary Science Letters*, v. 499, p. 1-12.
- 995 Lecumberri-Sanchez, P., Vieira, R., Heinrich, C., Pinto, F., and Walle, M., 2017, Fluid-rock  
996 interaction is decisive for the formation of tungsten deposits: *Geology*, vol. 45, p. 579–582.
- 997 Leisen M., Dubessy J., Boiron M.C., Lach P., 2012. Improvement of the determination of element  
998 concentrations in quartz-hosted fluid inclusions by LA-ICP-MS and Pitzer thermodynamic  
999 modeling of ice melting temperature. *Geochim. Cosmochim. Acta*, 90, 110-125.
- 1000 Lewis, A.J., Palmer, M.R., Sturchio, N.C., and Kemp, A.J., 1997, The rare earth element  
1001 geochemistry of acid-sulphate and acid-sulphate-chloride geothermal systems from  
1002 Yellowstone National Park, Wyoming, USA: *Geochimica et Cosmochimica Acta*, v. 61, p.  
1003 695-706.
- 1004 Linnen, R.L., and Cuney, M., 2005, Granite-related rare-element deposits and experimental  
1005 constraints on Ta-Nb- W-Sn-Zr-Hf mineralization, in Linnen, R.L. and Samson, I.M., eds.,  
1006 rare-element geochemistry and mineral deposits, Geological Association of Canada, Short  
1007 Course Notes, v. 17, p. 45-67.
- 1008 Llana-Funez, S., and Marcos, A., 2007, Convergence in a thermally softened thick crust: Variscan  
1009 intracontinental tectonics in Iberian plate rocks: *Terra Nova*, v. 19, p. 1-8.
- 1010 London, D., 2011, Experimental synthesis and stability of tourmaline: a historical overview: *The*  
1011 *Canadian Mineralogist*, v. 49, p. 117-136.
- 1012 Lourenço, A., 2002, Paleofluidos e mineralizações associadas às fases tardias da Orogenia  
1013 Hercínica: Unpublished PhD, Universidade do Porto, 326 p.
- 1014 Lüders, V., 1996, Contribution of infrared microscopy to fluid inclusion studies in some opaque  
1015 minerals (wolframite, stibnite, bournonite): *Metallogenic implications: ECONOMIC*  
1016 *GEOLOGY*, v. 91, p. 1462–1468.
- 1017 Ludwig, K.R., 2012, User's Manual for Isoplot 3.75, A Geochronological Toolkit for Microsoft  
1018 Excel: Berkeley Geochronology Center, Special Publication No. 5.
- 1019 Luvizotto, G.L, Zack, T., Meyer, H.P., Ludwig, T., Triebold, S., Kronz, A., Münker, C., Stockli,  
1020 D.F., Prowatke, S., Klemme, S., Jacob, D.E., and von Eynatten, H., 2009, Rutile crystals as  
1021 potential trace element and isotope mineral standards for microanalysis: *Chemical Geology*,  
1022 v., 261, p. 346-369.
- 1023 Marignac, C., Cuney, M. (2013) Past and present rare metal potential of Western Europe: In: PDAC  
1024 2013 (Toronto) Short Course "New Mines in the Old World: the untapped potential of  
1025 Europe".

- 1026 Marschall, H.R., and Jiang, S-Y., 2011, Tourmaline isotopes: No element left behind: *Elements*, v.  
1027 7, p. 313-319.
- 1028 Mateus, A., and Noronha, F., 2010, Sistemas mineralizantes epigenéticos na Zona Centro-Ibérica;  
1029 expressão da estruturação orogénica meso- a tardi-varisca (Epigenetic ore-forming systems in  
1030 Central-Iberian Zone; products of an evolving orogenic framework in meso- to late-Variscan  
1031 times): *Ciências Geológicas, Ensino, Investigação e sua História (Geologia Aplicada)*, v. 2, p.  
1032 47-61.
- 1033 Michaud J.A.-S., Gumiaux C, Pichavant, M., Gloaguen, E., Marcoux, E., 2020, From magmatic to  
1034 hydrothermal Sn-Li-(Nb-Ta-W) mineralization: The Argemela area (central Portugal): *Ore  
1035 Geology Reviews*, v. 116, <https://doi.org/10.1016/j.oregeorev.2019.103215>
- 1036 Nägler, T.F., Schäfer, H-J., and Gebauer, D., 1993, A new approach for the determination of the age  
1037 of partial or complete homogenization of Pb isotopes Example: anchimetamorphic, detrital  
1038 sediments of the Central Iberian Zone, Spain: *Chemical Geology*, v. 107, p. 191-199.
- 1039 Nägler, T.F., Schäfer, H-J., and Gebauer, D., 1995, Evolution of the Western European continental  
1040 crust: implications from Nd and Pb isotopes in Iberian sediments: *Chemical Geology*, v. 121,  
1041 p. 345-357.
- 1042 Neiva, A.M.R., 2002, Portuguese granites associated with Sn-W and Au mineralizations: *Bulletin  
1043 of the Geological Society of Finland*, v. 74, p. 79-101.
- 1044 Neiva, A.M.R., Silva, M.M.V.G., and Gomes, M.E.P., 2007, Crystal chemistry of tourmaline from  
1045 Variscan granites, associated tin-tungsten- and gold deposits, and associated metamorphic and  
1046 metasomatic rocks from northern Portugal: *Neues Jahrbuch für Mineralogie Abhandlungen*, v.  
1047 184, p. 45-76.
- 1048 Noronha, F., 2017, Fluids and Variscan metallogensis in granite related systems in Portugal:  
1049 Water-Rock Interaction International Symposium, 15<sup>th</sup>: *Procedia Earth and Planetary Science*,  
1050 v. 1, p. 1-4.
- 1051 Noronha, F., Dória, F., Dubessy, J., and Charoy, B., 1992, Characterization and timing of the  
1052 different types of fluids present in the barren and ore veins of the W-Sn deposit of  
1053 Panasqueira, central Portugal: *Mineralium Deposita*, v. 27, p. 72-79.
- 1054 Oosterom, M.G., Bussink, R.W., and Vriend, S.P., 1984, Lithogeochemical studies of aureoles  
1055 around the Panasqueira tin-tungsten deposit, Portugal: *Mineralium Deposita*, v. 19, p. 283-  
1056 288.
- 1057 Orejana, D., Villaseca, C., Pérez-Soba, C., López-García, J.A., and Billström, K., 2009, The  
1058 Variscan gabbros from the Spanish Central System: A case for crustal recycling in the sub-  
1059 continental lithospheric mantle?: *Lithos*, v. 110, p. 262-276.

1060 Paquette, J.L., Piro, J.-L., Devidal, J.-L., Bosse, V., Didier, A., Sannac, S., and Abdelhour, Y., 2014,  
1061 Sensivity enhancement in LA-ICP-MS by N<sub>2</sub> addition to carrier gas: application to  
1062 radiometric dating of U-Th -bearing minerals: *Agilent ICP-MS Journal*, v. 58, p; 4-5.

1063 Paton, C., Hellstrom, J., Bence, P., Woodhead, J., and Herg, J., 2011, Iolite: Freeware for the  
1064 visualisation and processing of mass spectrometric data: *Journal of Analytical Atomic*  
1065 *Spectrometry*, v. 26, p. 2508-2518.

1066 Pattison, D.R.M., 2001, Instability of Al<sub>2</sub>O<sub>5</sub> 'triple point' assemblages in muscovite+biotite+quartz  
1067 bearing metapelites, with implications: *American Mineralogist*, v. 86, p. 1414-1422.

1068 Pereira, M.F., Díez Fernández, R., Gama, C., Hofmann, M., Gärtner, A., and Linnemann, U., 2017,  
1069 S-type granite generation and emplacement during a regional switch from extensional to  
1070 contractional deformation (Central Iberian Zone, Iberian autochthonous domain, Variscan  
1071 Orogeny): *International Journal of Earth Sciences (Geologische Rundschau)*, DOI  
1072 10.1007/s00531-017-1488-3.

1073 Pereira Gómez, M.D., and Rodriguez Alonso, M.D., 2000, Duality of cordierite granites related to  
1074 melt-restite segregation in the Peña Negra anatectic complex, central Spain: *Canadian*  
1075 *Mineralogy*, v. 38, p. 1329-1346.

1076 Pérez-Cáceres, I., Martínez Poyatos, D., Fernando Simancas, J., and Azor, A., 2017, Testing the  
1077 Avalonian affinity of the South Portuguese Zone and the Neoproterozoic evolution of SW  
1078 Iberia through detrital zircon populations: *Gondwana Research*, v. 42, p. 177-192.

1079 Pinto, F., 2014, Estudo da distribuição do Estanho na Mina da Panasqueira: Mestrado em Geologia,  
1080 FCUP, Departamento de Geociências, Ambiente e Ordenamento do Território, 236 p.

1081 Poitrasson, F., Pin, C., and Duthou, J.-L., 1995, Hydrothermal remobilization of rare earth elements  
1082 and its effect on Nd isotopes in rhyolite and granite: *Earth and Planetary Science Letters*, v.  
1083 130, p. 1-11.

1084 Polya, D.A., 1989, Chemistry of the main-stage ore-forming fluids of the Panasqueira W–Cu(Ag)–  
1085 Sn deposit, Portugal: implications for models of ore genesis: *ECONOMIC GEOLOGY*, v. 84,  
1086 p. 1134–1152.

1087 Polya, D.A., Foxford, K.A., Stuart, F., Boyce, A., and Fallick, A.E., 2000, Evolution and  
1088 paragenetic context of low δD hydrothermal fluids from the Panasqueira W-Sn de- posit,  
1089 Portugal: new evidence from microthermometric, stable isotope, noble gas and halogen  
1090 analyses of primary fluid inclusions: *Geochimica et Cosmochimica Acta*, v. 64, p. 3357–  
1091 3371.

- 1092 Priem, H.N.A., and Den Tex, E., 1984, Tracing crustal evolution in the NW Iberian Peninsula  
1093 through the Rb-Sr and U-Pb systematics of Paleozoic granitoids: a review: *Physics of the*  
1094 *Earth and Planetary Interiors*, v. 35, p. 121-130.
- 1095 Renne, P.R., and Norman, E.B., 2001, Determination of the half-life of Ar-37 by mass  
1096 spectrometry: *Physical Review*, v. C, p. 6304-7302.
- 1097 Renne, P.R., Swisher, C.C., Deino, A.L., Karner, D.B., Owens, T.L., and DePaolo, D.J., 1998,  
1098 Inter-calibration of standards, absolute ages and uncertainties in  $^{40}\text{Ar}/^{39}\text{Ar}$  dating: *Chemical*  
1099 *Geology*, v. 145, p. 117-152.
- 1100 Renne, P.R., Cassata, W.S., and Morgan, L.E., 2009. The isotopic composition of atmospheric  
1101 argon and  $^{40}\text{Ar}/^{39}\text{Ar}$  geochronology: Time for a change?: *Quaternary Geochronology*, v. 4,  
1102 p. 288–298.
- 1103 Ribeiro, R.F., 2017, Gravimetric Modelling and Geological Interpretation of Argemela-Panasqueira  
1104 Area: PhD Thesis, Porto Universidad, 61 p.
- 1105 Roddick, J.C., 1983, High precision intercalibration of  $^{40}\text{Ar}/^{39}\text{Ar}$  standards: *Geochimica et*  
1106 *Cosmochimica Acta*, v. 47, p. 887-898.
- 1107 Rubio Pascual, F.J., Arenas, R., Martínez Catalán, J.R., Rodríguez Fernández, L.R., and Wijbrans,  
1108 J.R., 2013, Thickening and exhumation of the Variscan roots in the Iberian Central System:  
1109 Tectonothermal processes and  $^{40}\text{Ar}/^{39}\text{Ar}$  ages: *Tectonophysics*, v. 587, p. 207-221.
- 1110 Rubio Pascual, F.J., López-Carmona, A., and Arenas, R., 2016, Thickening vs. extension in the  
1111 Variscan belt: P–T modelling in the Central Iberian autochthon: *Tectonophysics*, v. 681, p.  
1112 144-158.
- 1113 Sant’Ovaia, H., Olivier, P., Ferreira, N., Noronha, F., and Leblanc, D., 2010, Magmatic structures  
1114 and kinematics emplacement of the Variscan granites from Central Portugal (Serra da Estrela  
1115 and Castro Daire areas): *Journal of Structural Geology*, v. 32, p. 1450-1465.
- 1116 Scarrow, J.H., Molina, J.F., Bea, F., Montero, P., and Vaughan, A.P.M., 2011, Lamprophyre dikes  
1117 as tectonic markers of late orogenic transtension timing and kinematics: A case study from the  
1118 Central Iberian Zone: *Tectonics*, v, 30(4): TC4007.
- 1119 Sluck, J.F., and Trumbull, R.B., 2011, Tourmaline as a recorder of ore-forming processes:  
1120 *Elements*, v. 7, p. 321-366.
- 1121 Snee, L.W., Sutter, J.F., and Kelly, W.C., 1988, Thermochronology of economic mineral deposits:  
1122 dating the stages of mineralisation at Panasqueira, Portugal, by high-precision  $^{40}\text{Ar}$ - $^{39}\text{Ar}$  age  
1123 spectrum techniques on muscovite: *ECONOMIC GEOLOGY*, v. 83, p. 335-354.
- 1124 Stacey, J.S., and Kramers, J.D., 1975, Approximation of terrestrial lead isotope evolution by a two-  
1125 stage model: *Earth and Planetary Science Letters*, v. 26, p. 207–221.

- 1126 Steiger, R.H., and Jäger, E., 1977, Subcommission on geochronology: Convention on the use of  
1127 decay constants in geo- and cosmochronology: *Earth and Planetary Science Letters*, v. 36, p.  
1128 359–362, doi: 10.1016/0012-821X(77)90060-7.
- 1129 Tang, H.-F., and Liu, C.-Q., 2002, Trace element geochemistry during metamorphic dehydration: A  
1130 case study from the Xingzi Group of Lushan, southeast China: *Geochemical Journal*, v.36, p.  
1131 545-561.
- 1132 Tornos, F., Delgado, A., Casquet, C., and Galindo, C., 2000, 300 Million years of episodic  
1133 hydrothermal activity: stable isotope evidence from hydrothermal rocks of the eastern Iberian  
1134 Central System: *Mineralium Deposita*, v. 35, p. 551–569.
- 1135 Valladares, M.I., Ugidos, J.M., Barba, P., and Colmenero, J.R., 2002, Contrasting geochemical  
1136 features of the Central Iberian Zone shales (Iberian Massif, Spain): implications for the  
1137 evolution of Neoproterozoic–Lower Cambrian sediments and their sources in other peri-  
1138 Gondwanan areas: *Tectonophysics*, v. 352, p. 121-132.
- 1139 van Hinsberg, V.J., 2011, Preliminary experimental data on trace-element partitioning between  
1140 tourmaline and silicate melt: *The Canadian Mineralogist*, v. 49, p. 153-163
- 1141 van Hinsberg, V.J., Henry, D.J., and Marschall, H.R., 2011, Tourmaline: an ideal indicator of its  
1142 host environment: *The Canadian Mineralogist*, v. 49, p.1-16.
- 1143 Vereshchagin, O.S., Frank-Kamenetskaya, O.V., Rozhdestvenskaya, I.V., and Zolotariev, A.A.,  
1144 2018, Incorporation of 3d elements in tourmalines: structural adjustments and stability:  
1145 *European Journal of Mineralogy*, v. 30, p. 917-928.
- 1146 Vermeesch, P., 2012, On the visualisation of detrital age distributions: *Chemical Geology*, v. 312-  
1147 313, p. 190-194, doi: 10.1016/j.chemgeo.2012.04.021.
- 1148 Vigne, J-L., André, G., and Kapal, F., 2018, Données industrielles, économiques, géographiques sur  
1149 les principaux produits chimiques, métaux, matériaux (11ème édition).  
1150 <http://www.societechimiquedefrance.fr/extras/Donnees/acc.htm>
- 1151 von Goerne, G., Franz, G., and Heinrich, W., 2001, Synthesis of tourmaline solid solutions in the  
1152 system  $\text{Na}_2\text{O} \pm \text{MgO} \pm \text{Al}_2\text{O}_3 \pm \text{SiO}_2 \pm \text{B}_2\text{O}_3 \pm \text{H}_2\text{O} \pm \text{HCl}$  and the distribution of Na between  
1153 tourmaline and fluid at 300 to 700 °C and 200 MPa: *Contributions to Mineralogy and  
1154 Petrology*, v. 141, p. 160-173.
- 1155 Weil, A.B., Gutiérrez-Alonso, G., Johnston, S.T., Pastor-Galán, D., 2013, Kinematic constraints on  
1156 buckling a lithospheric-scale orocline along the northern margin of Gondwana: A geologic  
1157 synthesis: *Tectonophysics*, v. 582, p. 25-49.
- 1158 Weisbrod, A., Polak, C., and Roy, D., 1986, Experimental study of tourmaline solubility in the  
1159 system Na–Mg–Al–Si–B–O–H. Applications to the boron content of natural hydrothermal

1160 fluids and tourmalinization processes: International Symposium on Experimental Mineralogy  
1161 and Geochemistry, Nancy, 1986, Abstracts, v. 140-141.

1162 Xu, J., Ding, R., Xie, Y., Zhong C., and Shan L., 2008, The source of hydrothermal fluids for the  
1163 Sarekoubu gold deposit in the southern Altai, Xinjiang, China: Evidence from fluid inclusions  
1164 and geochemistry: Journal of Asian Earth Sciences, v. 32, p. 247-258.

1165 Zack, T., Stockli, D.F., Luvizotto, G.L., Barth, M.G., Belousova, E., Wolfe, M.R., and Hinton,  
1166 R.W., 2011, In situ U-Pb rutile dating by LA-ICP-MS:  $^{208}\text{Pb}$  correction and prospects for  
1167 geological applications: Contributions to Mineralogy and Petrology, DOI 10.1007/s00410-  
1168 011-0609-4  
1169

## Appendix A0. Comparison of SEM-EDS and EPMA analyses of Panasqueira tourmaline

### 1. Problems in measuring Tur compositions by EPMA

The Pnq tourmaline crystals from the tourmalinized wall rocks are very small and therefore so are the different zones in the crystals. Owing to the rather low contrasting capacity of back scatter imaging by EPMA in our laboratory, it is usually challenging to assure that a given spot is really located in the desired zone: this is particularly true for the Tur 0 residual cores, that are usually not seen with EPMA. What is more, it is not so easy to retrieve under EPMA the crystals imaged by SEM - given that we ordinary explore the sections at random to find the best crystals.

For all these reasons, it was desirable to make measurements while identifying the zoning features, i.e., to mainly use SEM-EDS. To ensure compatibility of the two approaches, EPMA and SEM measurement were both performed on chosen crystals. Comparison between the results of the two kinds of measurement was thus made possible, and is effected in the following sections.

### 2. Reality and extent of a Si *apfu* bias in SEM-EDS analyses

As shown in Fig. A0-1, statistics of Si *apfu* from SEM-EDS analyses (calculated on an O, OH, F basis) display a shift towards values higher than 6.00, contrasting with the average 6.00 obtained from EPMA analyses.

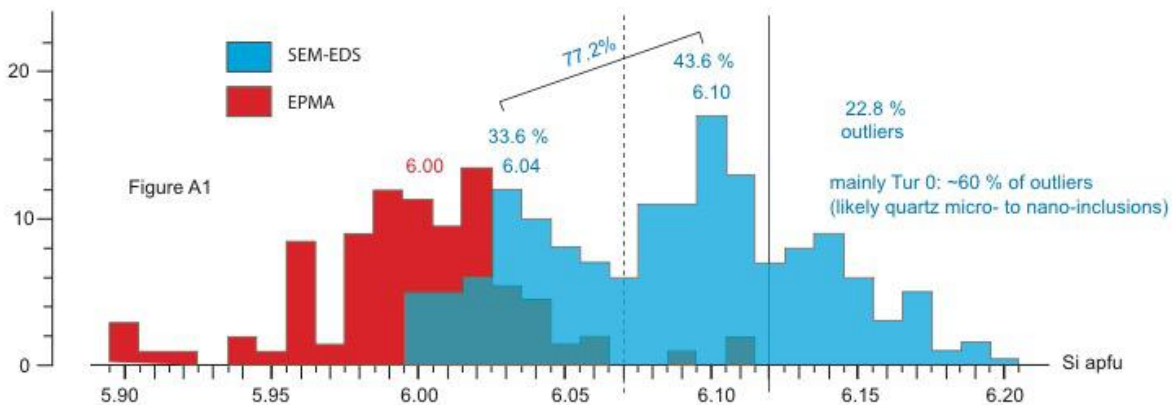


Figure A1. Comparative statistics of Si *apfu* measurements by EPMA or SEM-EDS.

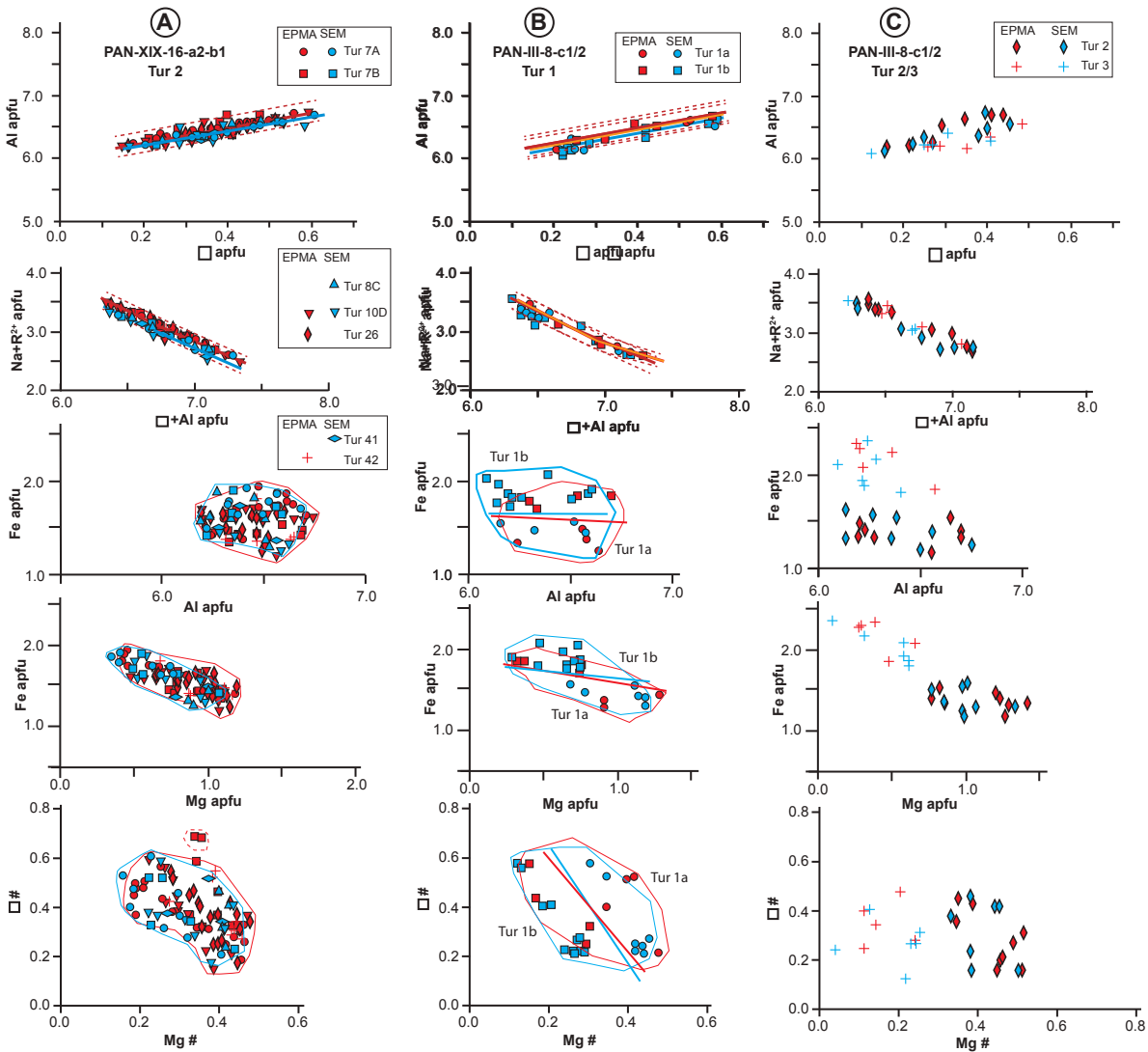
More precisely, the distribution is plurimodal, and ~ 35 % are comprised between 6.0 and 6.06 (averaging 6.04), ~ 45 % are comprised between 6.06 and 6.12 (averaging 6.10) and only ~20 % are higher; the latter are named “outliers” in the following. It may also be noted that there is a consistent overlap between the EPMA distribution and the first mode of the SEM-EDS distribution: in fact, EPMA distribution could be interpreted as bimodal, with the second mode nearly coincident with the first SEM-EDS mode.

It results that ~ 80 % of the SEM-EDS analyses yield lower than 6.12 Si *apfu* values, and it may be expected that this will cause only small shifts (if any) from the EPMA reference in the various crystal chemistry diagrams: this will be addressed in the following section.

Considering the outliers, it appears that most of them (~ 60 %) come from the Tur0 relict cores. A possible explanation of such deviant analyses could be the presence in the cores of nano-inclusions of quartz crystals: as mentioned in the main text, many tourmaline crystals of the tourmalinized wall-rocks are clouded of quartz inclusions, often concentrated in the core zones. If so, the formula calculation should not affect too much the elemental ratios, and it may be expected that plotting of the analyses in the various diagrams will reveal the same trends as the “cleaner” analyses. This will be examined in a following section.

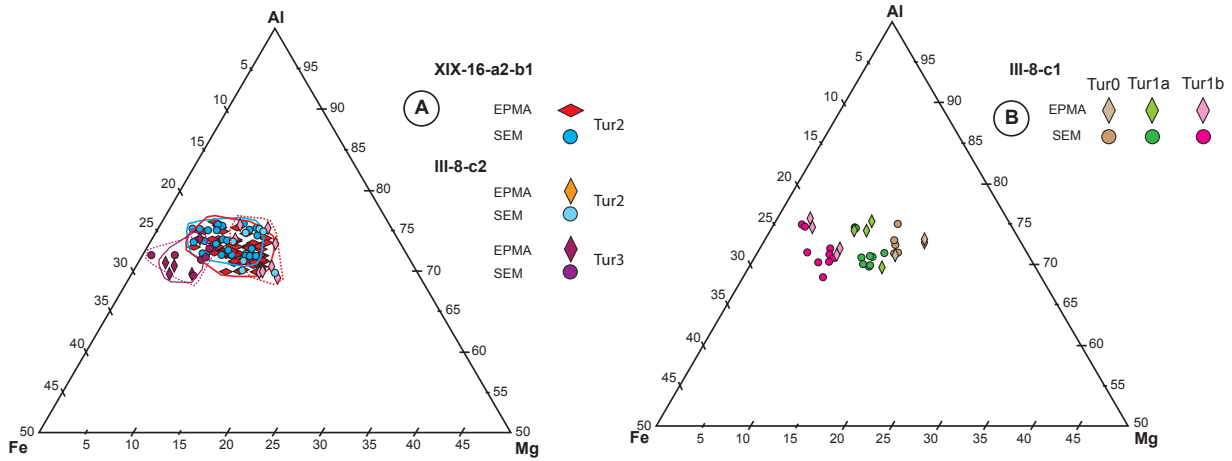
### 3. SEM-EPMA comparison

1210 For the comparison, the more suitable crystals, of sufficiently large size, appear to belong to a  
 1211 second generation of tourmaline (Tur2), **not addressed in the manuscript**, of which two sets of  
 1212 crystals were available, in samples PAN XIX-16-a2-b1 and PAN-III-8-c1/2; in the latter, however,  
 1213 sufficiently contrasted zoned crystals of the first generation (Tur1) found in crack-seal quartz  
 1214 veinlets (see Figure 4 in main text) could also be measured by the two method, as well as late  
 1215 (Tur3) overgrowths on Tur2.



1216 **Figure A2.** Comparison of EPMA and SEM-EDS measurements on selected sets of tourmaline crystals in two samples  
 1217 (see text).  
 1218  
 1219

1220 Comparison is made in a series of diagrams in Fig. A0-2, and results are the following:  
 1221 - the diagram characteristics (range of values, distribution of Tur types) are basically the  
 1222 same for the two sets of analyses;  
 1223 - very limited shifts affect the trends in the Al vs [] and Na+R<sup>2+</sup> vs Al+[] diagrams for  
 1224 SEM-EDS analyses relative to EPMA ones: nevertheless, the SEM-EDS trends remain included  
 1225 in the dispersion field of EPMA analyses;  
 1226 - the Al/Fe/Mg ratios seem in particular identical in the two sets of results; this is  
 1227 confirmed by examination of the AFM diagrams in Fig. A0-3. It is noteworthy that the  
 1228 dispersion of the Al/Fe+Mg ratios is similar whatever the analysis **method**, thus certifying that  
 1229 this dispersion is real.  
 1230 It may thus be concluded that use of SEM-EDS analyses in place of EPMA ones for the considered  
 1231 crystals did not affect the restitution of crystal chemistry properties.

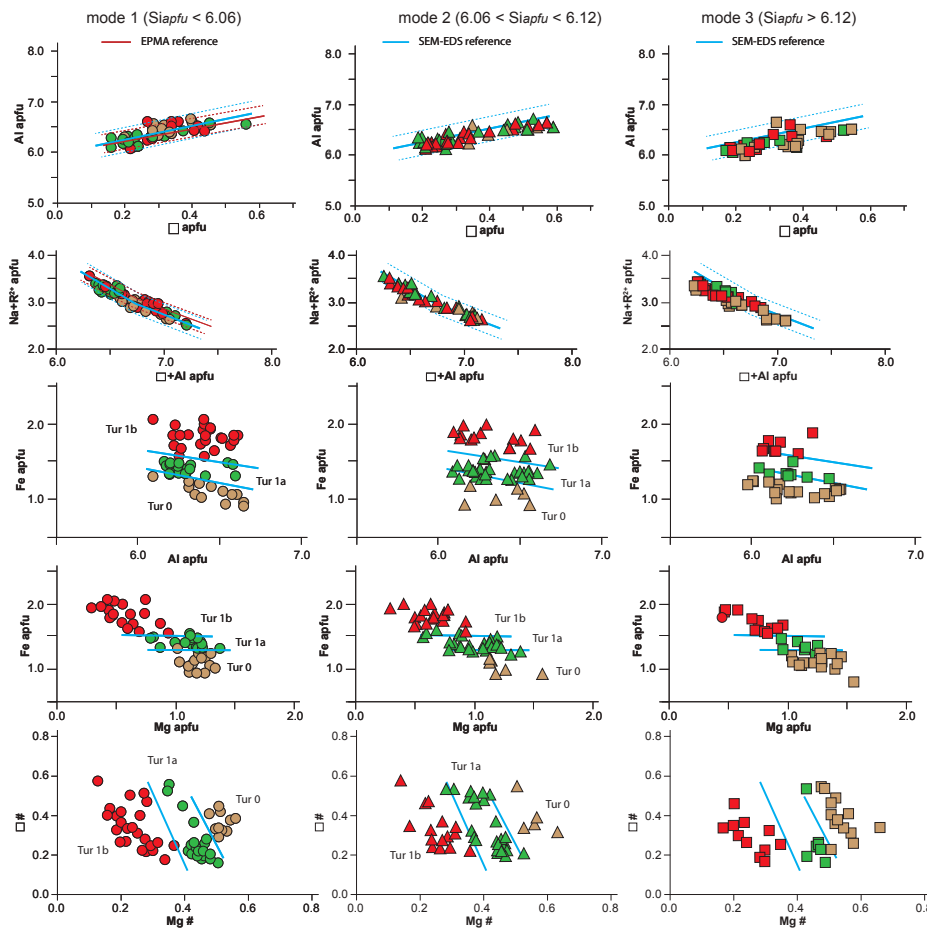


1232  
1233  
1234  
1235  
1236  
1237  
1238  
1239

**Figure A3.** Comparison of EPMA and SEM-EDS analyses in AFM diagrams. **A:** Tur2 (samples PAN-XIX-16-a2-b1 and PAN-III-8-c2) and Tur3 (PAN-III-8-c2; **B:** Tur 0 and Tur 1 (sample PAN-III-8-c1, excepted Tur0-EPMA, taken from other samples).

#### 4. Internal consistency of SEM-EDS analyses

Separating the analyses in three sets corresponding to the three modes in Fig. A0-1 (mode 1 = “low” Si, mode 2 = “high” Si, mode 3 = “outliers”) is done in the diagrams of Fig. A0-4 and



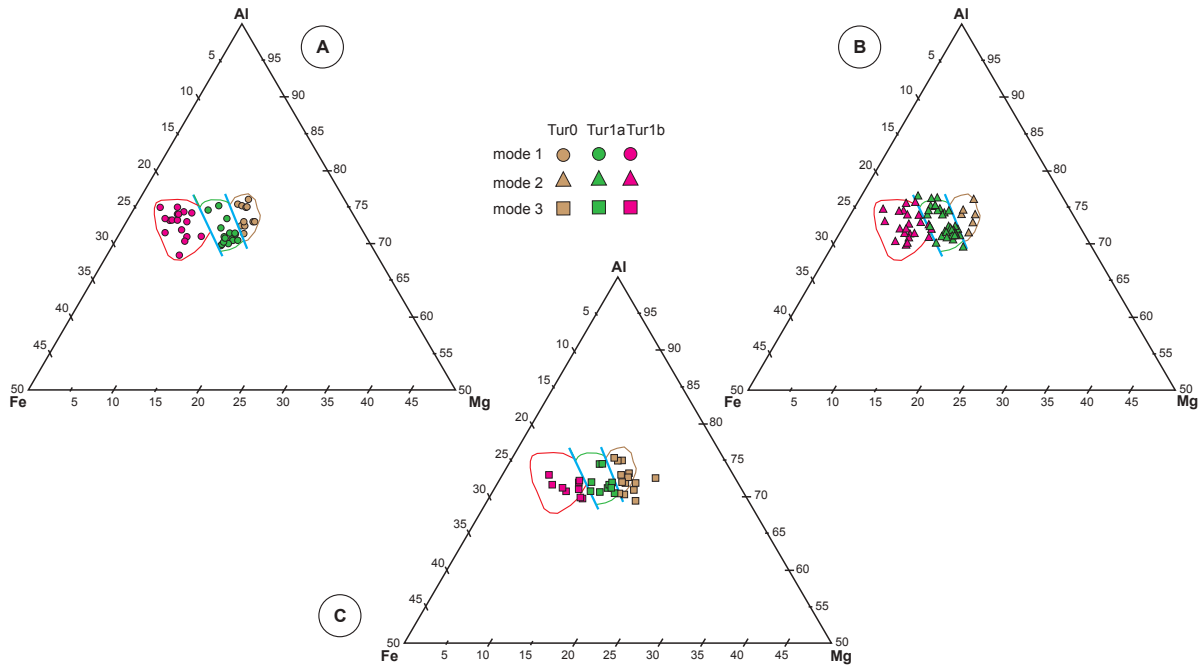
1240  
1241  
1242  
1243  
1244  
1245  
1246

**Figure A0-4.** Checking the internal consistency of SEM-EDS analyses using classical crystal chemistry diagrams. The domain boundaries are those corresponding to mode 1 in all diagrams. The red lines correspond to EPMA reference.

**A0-5.**  
(i) A first result is that in the Al vs [] and Na+R<sup>2+</sup> vs Al+[] diagrams, the whole of the mode 1 values behave as the ones in sample III-8-c, as indeed expected. The crystal chemistry diagrams of these mode 1 analyses may thus be in turn used as reference for the other sets of analyses.

1247 (ii) In all the diagrams, the mode 2 values yield basically the same relations, and in particular,  
 1248 the boundaries between “Tur0”, “Tur1a” and “Tur1b” fields are very consistent in the three Fe vs.  
 1249 Al, Fe vs Mg and []# vs. Mg# diagrams in Fig. A0-4, and in the AFM diagrams in Fig. A0-5.

1250 (iii) As expected, the “outlier” values are shifted in the Al vs [] and Na+R<sup>2+</sup> vs Al+[] diagrams,  
 1251 displaying nevertheless the same characteristics. They however are highly compatible with the  
 1252 preceding sets of values in the other diagrams. This is particularly significant for the Tur0 values.  
 1253



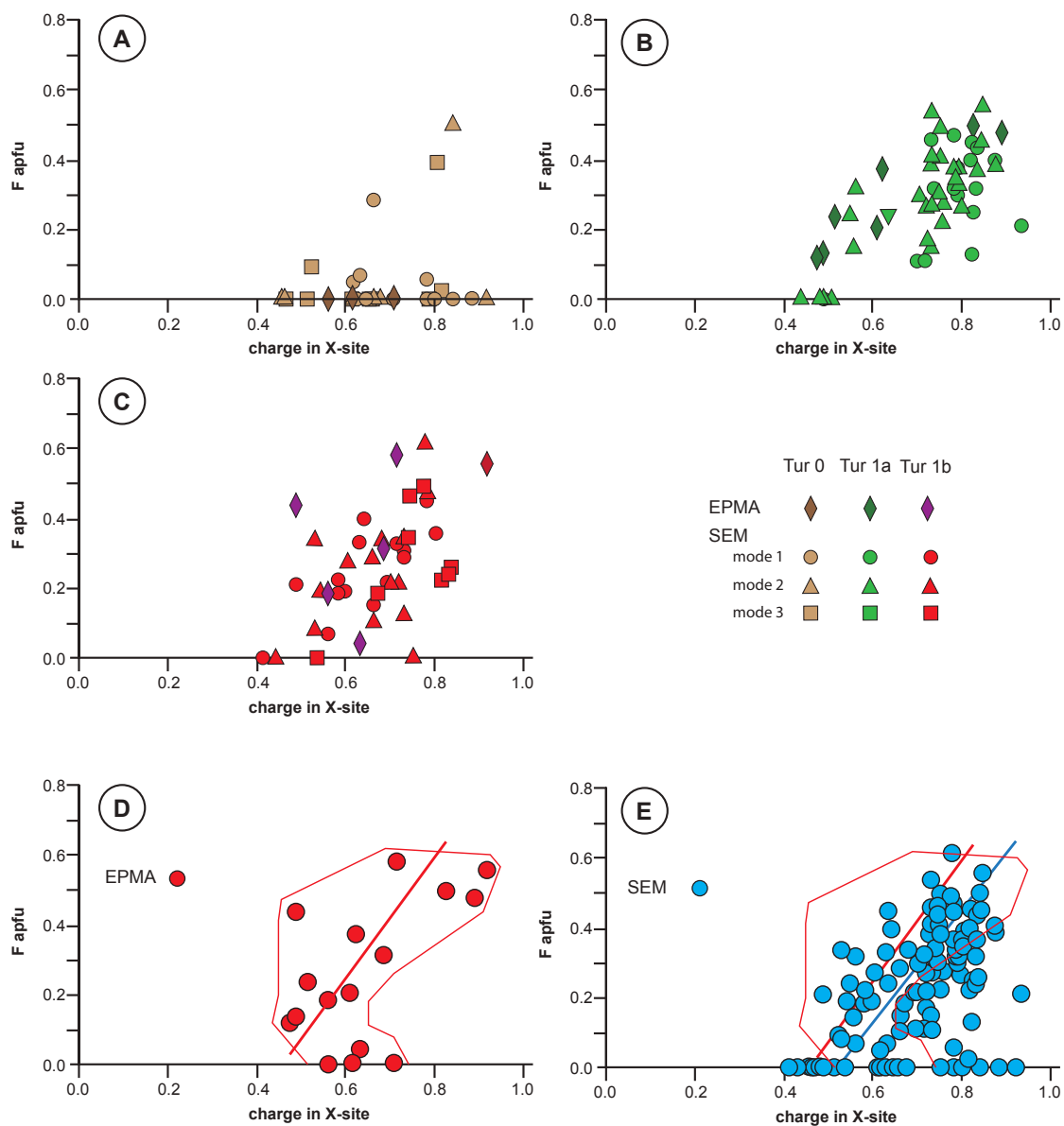
1254 **Figure A0-5.** Checking the internal consistency of SEM-EDS analyses in the AFM triangle. A: mode 1 ("low Si");  
 1255 B: mode 2 ("high Si"); C: mode 3 ("outliers"). The domain boundaries are those corresponding to mode 1 in all three  
 1256 diagrams.  
 1257  
 1258

1259 **5. The case for F**

1260 It is known that, in tourmaline, there may be a rough linear relationships between F content and the  
 1261 ionic charge associated with the site X infilling. Consideration of Fig. A0-6 shows that this is  
 1262 indeed the case and that:

- 1263 - (i) there is no significant differences between the SEM-EDS analyses corresponding to  
 1264 either mode 1, or mode 2 or mode 3 of the Si distribution (Fig. A0-6A to C)
- 1265 - (ii) the scarcity of EPMA measurements in Tur 1 prevents a comparison zone by zone,  
 1266 although the rare Tur0 measurements by EPMA confirm that F content in Tur0 id generally low  
 1267 (Fig. A0-6A)
- 1268 - (iii) if therefore EPMA and SEM-EDS analyses are considered as a whole (Fig. A0-6D and  
 1269 E), both sets of analyses display a large dispersion and a very rough linear relationship, with a slight  
 1270 difference between the two sets which nevertheless does not introduce a significant difference for  
 1271 the data interpretation.

1272  
 1273



1274  
 1275  
 1276  
 1277  
 1278  
 1279  
 1280  
 1281  
 1282  
 1283

**Figure A0-6.** Relationships between F and the X-site charge: comparison of EPMA and SEM-EDS results. A to C: comparison zone by zone (A: Tur0; B: Tur 1a; C: Tur 1b); D-E: bulk comparison. Contours in E: from D

## 6. Conclusion

It results from the preceding that the SEM-EDS analyses may be safely used for the crystal chemistry characterization of the Panasqueira tourmaline, provided that analyses from mode 3 group be discarded.

Finally, 117 spots in 19 samples are taken into consideration in the main text.

## Appendix A1-Table A1: Operating conditions for the LA-ICP-MS equipment

<b>Laboratory &amp; Sample Preparation</b>	
Laboratory name	Géosciences Rennes, UMR CNRS 6118, Rennes, France
Sample type/mineral	Rutile
Sample preparation	Rutile grains in context in thin-sections
Imaging	JEOL J7600F scanning electron microscope (SEM)
<b>Laser ablation system</b>	
Make, Model & type	ESI NWR193UC, Excimer
Ablation cell	ESI NWR TwoVol2
Laser wavelength	193 nm
Pulse width	< 5 ns
Fluence	8.0 J/cm <sup>2</sup>
Repetition rate	5 Hz
Spot size	45 µm (round spot)
Sampling mode / pattern	Single spot
Carrier gas	100% He, Ar make-up gas and N <sub>2</sub> (3 ml/min) combined using in-house smoothing device
Background collection	20 seconds
Ablation duration	60 seconds
Wash-out delay	15 seconds
Cell carrier gas flow (He)	0.75 l/min
<b>ICP-MS Instrument</b>	
Make, Model & type	Agilent 7700x, Q-ICP-MS
Sample introduction	Via conventional tubing
RF power	1350W
Sampler, skimmer cones	Ni
Extraction lenses	X type
Make-up gas flow (Ar)	0.87 l/min
Detection system	Single collector secondary electron multiplier
Data acquisition protocol	Time-resolved analysis
Scanning mode	Peak hopping, one point per peak
Detector mode	Pulse counting, dead time correction applied, and analog mode when signal intensity > ~ 10 <sup>6</sup> cps
Masses measured	<sup>204</sup> (Hg + Pb), <sup>206</sup> Pb, <sup>207</sup> Pb, <sup>208</sup> Pb, <sup>232</sup> Th, <sup>238</sup> U
Integration time per peak	10-30 ms
Sensitivity / Efficiency	25000 cps/ppm Pb (50µm, 10Hz)
Dwell time per isotope	5-70 ms depending on the masses
<b>Data Processing</b>	
Gas blank	20 seconds on-peak
Calibration strategy	R10 Rutile used as primary reference material, R19 rutile used as secondary reference material (quality control)
Reference Material info	R10 (Luvizotto et al., 2009) R19 (Zack et al., 2011)
Data processing package used	Iolite (Paton et al., 2010), VizualAge_UcomPbine (Chew et al., 2014)
Quality control / Validation	R19: Apr 2016: 490 ± 3.4 Ma (MSWD=1.11; N=13) Dec 2017 : 493 ± 12 Ma (MSWD=2; N=12)

## Appendix A2: Ar-Ar dating of muscovite (methodology)

Argon isotopes (from mass 40 to 37) were measured using Faraday detectors with low noise  $1 \times 10^{12} \Omega$  resistors and mass 36 was measured using a compact discrete dynode (CDD) detector. The sensitivity for argon measurements is  $\sim 6.312 \times 10^{17}$  moles/fA as determined from measured aliquots of Fish Canyon Sanidine (Dazé et al., 2003; Kuiper et al., 2008). Standards and sample were placed in 2 mm deep wells in 18 mm diameter aluminium disks, with standards placed strategically so that the lateral neutron flux gradients across the disk could be evaluated. Planar regressions were fit to the standard data, and the  $^{40}\text{Ar}/^{39}\text{Ar}$  neutron fluence parameter (J) interpolated for the unknowns. Uncertainties in J are estimated at 0.1 - 0.2% ( $1 \sigma$ ), based on Monte Carlo error analysis of the planar regressions (Best et al., 1995). All specimens were irradiated in the Cadmium-lined, in-core CLICIT facility of the TRIGA reactor at the Oregon State University (USA). The duration of irradiation was 17 hours and using the Fish Canyon sanidine (Kuiper et al., 2008) and GA1550 biotite (Spell and McDougall, 2003) standards. Standards for  $^{40}\text{Ar}/^{39}\text{Ar}$  measurements were placed in a Cu sample tray, with a KBr cover slip, in a stainless steel chamber with a differentially pumped ZnS viewport attached to a Thermo Fisher Scientific extraction/purification line and baked with an infrared lamp for 24 hours. Single crystals were fused using the  $\text{CO}_2$  laser. The sample selected for the  $^{40}\text{Ar}/^{39}\text{Ar}$  dating has been previously investigated by optical microscopy and SEM in order to spot homogeneous areas devoid of alteration, micro-inclusions or internal zoning. Discs of 5 mm in diameter and  $\sim 150 \mu\text{m}$  thick were cut from the same polished thick section (150 - 200  $\mu\text{m}$  thick). The discs were mounted using a ceramic adhesive (PELCO) on a quartz slide placed in a stainless steel chamber with a sapphire viewport attached to the same stainless steel high vacuum extraction system as the  $\text{CO}_2$  laser, and baked with an infrared lamp for 48 hours. For this study, a raster size of about 100 x 100  $\mu\text{m}$  was used and ablation pits were excavated to an estimated depth of 50  $\mu\text{m}$ . Reactive gases were removed for both the standard and unknown, after 3 minutes, by three GP-50 SAES getters (two at room temperature and one at 450 °C) prior to being admitted to an ARGUS VI mass spectrometer by expansion. Five argon isotopes were measured simultaneously over a period of 6 minutes.

### *References cited*

Best, M.G., Christiansen, E.H., Deino, A.L., Grommé, C.S., and Tingey, D.G., 1995, Correlation and emplacement of a large, zoned, discontinuously exposed ash-flow sheet: Ar/ Ar 40 39 chronology, paleomagnetism, and petrology of the Pahranaagat Formation, Nevada: Journal of Geophysical Research, v. 100, p. 24,593-24,609.

- 1321 Dazé, A., Lee, J.K.W., and Villeneuve, M., 2003, An intercalibration study of the Fish Canyon  
1322 sanidine and biotite  $^{40}\text{Ar}/^{39}\text{Ar}$  standards and some comments on the age of the Fish Canyon  
1323 Tuff: *Chemical Geology*, v. 199, p. 111–127.
- 1324 Kuiper, K.F., Deino, A., Hilgen, F.J., Krijgsman, W., Renne, P.R., and Wijbrans, J.R., 2008,  
1325 Synchronizing the rock clocks of Earth history: *Science*, v. 320, p. 500–504.
- 1326 Spell, T.L., and McDougall, I., 2003, Characterization and calibration of  $^{40}\text{Ar}/^{39}\text{Ar}$  dating standards:  
1327 *Chemical Geology*, v. 198, p. 189–211..  
1328

## Appendix A8: Mass balance calculations

1329  
1330  
1331  
1332  
1333  
1334  
1335  
1336  
1337  
1338  
1339  
1340  
1341  
1342  
1343  
1344  
1345  
1346  
1347  
1348  
1349  
1350  
1351  
1352  
1353  
1354  
1355  
1356  
1357  
1358  
1359  
1360  
1361  
1362

### *Boron mass balance calculations*

*Boron endowment in the granites:* It must be emphasized that the greisenized cupola and the subjacent granites layer are typically devoid of tourmaline, meaning that the original melts were not tourmaline saturated. This raises the question of these granites being a boron source for the Panasqueira system. In any case, these granites being of the RMG family, and their solidus temperature being accordingly in the c. 600°-650°C range (Aksyuk and Konyshev, 2011), their boron content could not have been higher than the equilibrium B content in equilibrium with tourmaline in the melt at these temperatures, i.e., no more than 0.5 wt% B<sub>2</sub>O<sub>3</sub> (London, 2011; and references therein). The volume of the cupola itself (approximated by a cone, high 150 m, diameter 250 m) being of  $\sim 2.5 \cdot 10^6 \text{ m}^3$ , it could not contain more than  $\sim 9 \text{ kt B}$  (with a melt density of  $2.3 \text{ t.m}^{-3}$ ; Dingwell et al., 1993). The subjacent RMG sheet-like body, made of several separate intrusions (De Amorin, 2017), may be approximated as a 100 m thick body with about  $1 \text{ km}^2$  surface (Fig. 2), yielding a  $\sim 10^8 \text{ m}^3$  volume and a maximal content of 360 kt B. Thus, the total possible boron yield by the evolved granites could not have exceeded 370 kt B.

*Boron required for the wall-rock tourmalinization:* These values must be compared with the B content in the tourmalinized wall-rock. (i) At the single vein scale, we consider an average vein system based onto the description by Foxford et al. (2000, their Fig.8): an elliptical area (minor axis  $\sim 100 \text{ m}$ , major axis  $\sim 300 \text{ m}$ ), a total width of the tourmalinized margins of 0.45 m (i.e., 15 cm on one side of the vein and 30 cm on the other) and an averaged 50 volume % of tourmaline in the altered zones. This yields a unitary volume of the altered zone of  $\sim 1.1 \cdot 10^4 \text{ m}^3$ . Adopting an average density of  $3.1 \text{ t.m}^{-3}$ , and a boron content of 3.3% for the tourmaline, this unitary volume contains  $\sim 540 \text{ t B}$ . (ii) The number of elementary veins may be estimated using the published values for the total volume of the vein system, between 3 and  $6 \cdot 10^3 \text{ km}^3$  (Polya, 1989), and assuming an average vein thickness of 0.2 m (Foxford et al., 2000). This yields an estimated number of elementary veins comprised between 750 and 1500. (iii) Finally, the total B content of the tourmalinized wall rocks may be bracketed between 410 and 810 kt. These values are clearly higher than the maximum boron tonnage possibly delivered by the Panasqueira RMG.

### *Volume of magmatic water required for boron transportation*

At the elementary vein scale, and at any time of the tourmalinization process, the effective volume of fluid present in the  $V_0$  volume of altered rocks (estimated at  $1.2 \cdot 10^4 \text{ m}^3$ , see above) is controlled by rock porosity. If  $\phi$  is the porosity, this effective volume is only  $\phi \cdot V_0$ . The porosity of

1363 metamorphic rocks is generally considered to be in the  $10^{-1}$  to  $10^{-2}$  range (Bickle and McKenzie  
1364 1987), and was for instance estimated at 0.08 in the Tinos schists (Breeding et al., 2003). Here, we  
1365 take  $\phi=0.1$ . The effective  $\phi.V_0$  volume contains a boron mass  $m_0 = \phi.V_0.\rho_w.X$ , with  $\rho_w$  the fluid  
1366 density and  $X$  the boron content in the fluid. For a magmatic fluid equilibrated with tourmaline at  
1367 the solidus temperature, the boron content  $X$  will be close to 1 wt %  $B_2O_3$  (Weisbrod et al., 1986)  
1368 and the fluid density will be in the 0.62-0.68  $t.m^{-3}$  range, depending on salinity between  $\sim 10$  and  
1369  $\sim 20$  wt% NaCl (Sakuma and Ichiki, 2016); taking an average 0.65 yields  $m_0= 2$  t B. Therefore, to  
1370 attain the 540 t B accumulated in the tourmalinized wall rock, the  $\phi.V_0$  volume must be renewed  
1371  $540/2=270$  times, i.e., a total flow of  $270.\phi.V_0= 2.9.10^6$   $m^3$  of fluid must be channelled through the  
1372 transforming schist. At the deposit scale, this in turn means that a volume of fluid comprised  
1373 between  $2.2.10^9$  and  $4.3.10^9$   $m^3$  was required for the tourmalinization be effective.

#### 1374 *Possible water yield by the granite system*

1375 The water content of a RMG melt is  $\sim 5$  wt%. Thus, the Panasqueira RMG sheet-like body, with a  
1376 volume of  $10^8$   $m^3$  and a melt density of  $2.3$   $t.m^{-3}$ , contained about  $1.2.10^7$  t water, i.e. (with a water  
1377 density of  $0.65$   $t.m^{-3}$ ) could have expelled  $\sim 1.8.10^7$   $m^3$  of fluid. This is clearly two orders of  
1378 magnitude below the required fluid quantity. It must be noted that it is the same for the main  
1379 wolframite deposition stage, as already stated by Polya (1989), who estimated a several  $100$   $km^3$   
1380 (up to 1000) flow to produce the deposit. This was however based on a 0.2 ppm W content in the  
1381 fluid, which was clearly underestimated: owing to the data of Wood and Vlassopoulos (1989), a  
1382 content of  $\sim 500$  ppm W is more realistic, and would demand a volume of  $\sim 5.10^8$   $m^3$  to yield the c.  
1383 150 kt of W of the deposit, one order of magnitude larger than the granite water endowment.

1384

#### 1385 *Metasediments as a source of boron and fluid*

1386 The Beira schists contain in average  $\sim 100$  ppm B (Oosterom et al., 1984). With this content, and  
1387 assuming a density for the schist of  $2.77$   $t.m^{-3}$  (Ribeiro, 2017), a schist volume of  $1.7$   $km^3$  to  $3.4$   
1388  $km^3$  is required, admitting a 100% efficient extraction, which is not so likely. However, the few  
1389 data available for the high grade Beira schists (Peña Negra migmatitic complex, Acosta-Vigil et al.,  
1390 2011) suggest that boron extraction may have reached 70% efficiency. With this value, the needed  
1391 volumes become comprised between  $2,8$   $km^3$  and  $4,8$   $km^3$ . On the other hand, to yield the volume of  
1392 fluid required by the boron transportation and deposition (see above), assuming a water productivity  
1393 of about 3 wt % (Fyfe et al., 1978), between  $20$   $km^3$  and  $40$   $km^3$  of schist are necessary. The source  
1394 of boron and fluids for the tourmalinization at Panasqueira could therefore have been the Beira  
1395 schists.

1396

1397 *References cited*

- 1398 Acosta-Vigil, A., Pereira, M.D., Shaw, D.M., and London, D., 2011, Contrasting behaviour of  
1399 boron during crustal anatexis: *Lithos*, v. 56, p. 15-31.
- 1400 Bickle, M.J., and McKenzie, D., 1987, The transport of heat and matter by fluids during  
1401 metamorphism: *Contributions to Mineralogy and Petrology*, v. 95, p. 384-392.
- 1402 Breeding, C.M., Ague, J.J., Brocker, M., and Bolton, E.W., 2003, Blueschist preservation in a  
1403 retrograded, high-pressure, low-temperature metamorphic terrane, Tinos, Greece:  
1404 implications for fluid flow paths in subduction zones: *Geochemistry Geophysics Geosystems*,  
1405 v. 4, 1: 9002, doi: 10.1029/2002GC000380.
- 1406 De Amorin, A., 2017, Pétrographie géochimie des granitoides de la mine de W de Panasqueira  
1407 (Portugal): Rôle dans la genèse des minéralisations: Unpublished M.Sc. thesis, Université de  
1408 Lorraine (France), Laboratoire Géoressources, 37 p.
- 1409 Dingwell, D.B., Knoche, R., and Webb, S.L., 1993, The effect of F on the density of haplogranite  
1410 melt: *American Mineralogist*, v. 78, p. 325-330.
- 1411 Foxford, K.A., Nicholson, R., Polya, D.A., and Hebblethwaite, R.P.B., 2000, Extensional failure  
1412 and hydraulic valving at Minas da Panasqueira, Portugal: evidence from vein spatial  
1413 distributions, displacements and geometries: *Journal of Structural Geology*, v. 22, p. 1065–  
1414 1086, [http://dx.doi.org/10.1016/S0191-8141\(00\)00029-8](http://dx.doi.org/10.1016/S0191-8141(00)00029-8).
- 1415 Fyfe, W.S., Price, N.J., and Thompson, A.B., 1978, *Fluids in the earth's crust*. Amsterdam: Elsevier,  
1416 389 p.
- 1417 Oosterom, M.G., Bussink, R.W., and Vriend, S.P., 1984, Litho-geochemical studies of aureoles  
1418 around the Panasqueira tin-tungsten deposit, Portugal: *Mineralium Deposita*, v. 19, p. 283-  
1419 288.
- 1420 Polya, D.A., 1989, Chemistry of the main-stage ore-forming fluids of the Panasqueira W–Cu(Ag)–  
1421 Sn deposit, Portugal: implications for models of ore genesis: *ECONOMIC GEOLOGY*, v. 84,  
1422 p. 1134–1152.
- 1423 Ribeiro, R.F., 2017, Gravimetric Modelling and Geological Interpretation of Argemela-Panasqueira  
1424 Area: PhD Thesis, Porto Universidad, 61 p.
- 1425 Sakuma, H., and Ichiki, M., 2016, Density and isothermal compressibility of supercritical H<sub>2</sub>O–  
1426 NaCl fluids: molecular dynamics study from 673 to 2000 K, 0.2 to 2 GPa, and 0 to 22 wt%  
1427 NaCl: *Geofluids*, v. 16, p. 89-102.
- 1428 Weisbrod, A., Polak, C., and Roy, D., 1986, Experimental study of tourmaline solubility in the  
1429 system Na–Mg–Al–Si–B–O–H. Applications to the boron content of natural hydrothermal

1430 fluids and tourmalinization processes: International Symposium on Experimental Mineralogy  
1431 and Geochemistry (Nancy), Abstracts, v. 140-141.  
1432 Wood, S.A., and Vlassopoulos, D., 1989, Experimental determination of the solubility and  
1433 speciation of tungsten at 500 °C and 1 kbar: *Geochimica et Cosmochimica Acta*, v. 53, p.  
1434 303–312.